Multi-Source Acoustic Arrays Induce Volumetric Bulk Cracking in Stone Analogues: A Phase-Field Computational Study with Implications for Next-Generation Lithotripters

Mohammad Yaghoub Abdollahzadeh Jamalabadi *

Posted Date: 28 May 2026

doi: 10.20944/preprints202605.1906.v1

Keywords: lithotripsy; symmetric spherical blast; phase-field fracture; shock wave lithotripsy; heavy metals; crack propagation; acoustic-structure interaction; kidney stones

 doi:10.20944/preprints202605.1906.v1

Article

Multi-Source Acoustic Arrays Induce Volumetric Bulk Cracking in Stone Analogues: A Phase-Field Computational Study with Implications for Next-Generation Lithotripters

Mohammad Yaghoub Abdollahzadeh Jamalabadi

Department of Mechanical Engineering, Chabahar Maritime University Chabahar 99717, Iran; my.abdollahzadeh@cmu.ac.ir

Abstract

Background: Extracorporeal shock wave lithotripsy (ESWL) remains a non-invasive option for urolithiasis, but its stone-free rates are inferior to endoscopic alternatives, particularly for dense calculi. The physical mechanisms governing shock-wave-induced fracture—especially the role of multi-source acoustic arrays—are incompletely understood. Furthermore, the presence of heavy metals (e.g., cadmium, lead, arsenic) in some kidney stones may increase fragmentation resistance. **Methods:** We conducted a systematic synthesis of 22 meta-analyses comparing ESWL, ureteroscopic laser lithotripsy (URSL), retrograde intrarenal surgery (RIRS), and percutaneous nephrolithotomy (PCNL). Separately, we developed a novel axisymmetric phase-field damage model coupling nonlinear pressure acoustics in water with elastodynamics in a heavy metal stone analogue, incorporating acoustic-structure interaction and Ginzburg–Landau fracture evolution. Simulations compared single-monopole versus ten-monopole source configurations. **Results:** Clinical synthesis confirms that ESWL has the lowest complication rate (RR 0.58, 95% CI 0.51–0.66) but significantly lower stone-free rates than RIRS (RR 0.57) and URSL (RR 0.58). Computationally, the ten-source array produced constructive interference that shifted peak von Mises stress from the fluid-solid interface to the stone center. This altered the fracture mechanism from surface-dominated spallation to volumetric bulk cracking, increasing the phase-field damage volume fraction by approximately 300% and promoting finer fragmentation ("dusting"). Heavy metal content (Cd, Pb, As) correlated with increased stone risk (19–69% higher odds) and may also reduce fragmentation efficiency. **Conclusions:** Multi-source acoustic arrays fundamentally improve stone comminution by inducing volumetric bulk cracking rather than surface spallation. This computational evidence supports the design of next-generation lithotripters with multiple, phased sources to achieve higher stone-free rates while preserving the low complication profile of ESWL. Integration of stone density, heavy metal content, and array configuration may enable personalized shock wave protocols.

Keywords: lithotripsy; symmetric spherical blast; phase-field fracture; shock wave lithotripsy; heavy metals; crack propagation; acoustic-structure interaction; kidney stones

1. Introduction

Urinary stone disease affects approximately one in ten people in the United States and accounts for an estimated annual healthcare cost of $10 billion. The lifetime risk of developing a kidney stone is approximately 10–15%, and recurrence rates are high, necessitating effective and safe treatment options. The landmark introduction of the Dornier HM3 lithotripter in the early 1980s marked a paradigm shift in the management of urolithiasis. For the first time, stones could be fragmented without any surgical incision, using focused shock waves generated externally and transmitted through the body. ESWL quickly became the dominant non-invasive treatment modality for renal

 doi:10.20944/preprints202605.1906.v1

and ureteral stones. However, as clinical experience accumulated, limitations became apparent: stone-free rates (SFRs) vary considerably with stone size, composition, and location; the need for retreatment is not negligible; and complications such as renal hematoma, steinstrasse, and infection may occur. Lithotripsy is a noninvasive procedure used to treat kidney stones that are too large to pass through the urinary tract (the skin is not pierced). Schematic of shock wave production for extracorporeal shock wave lithotripsy for kidney stone shown in Figure 1.

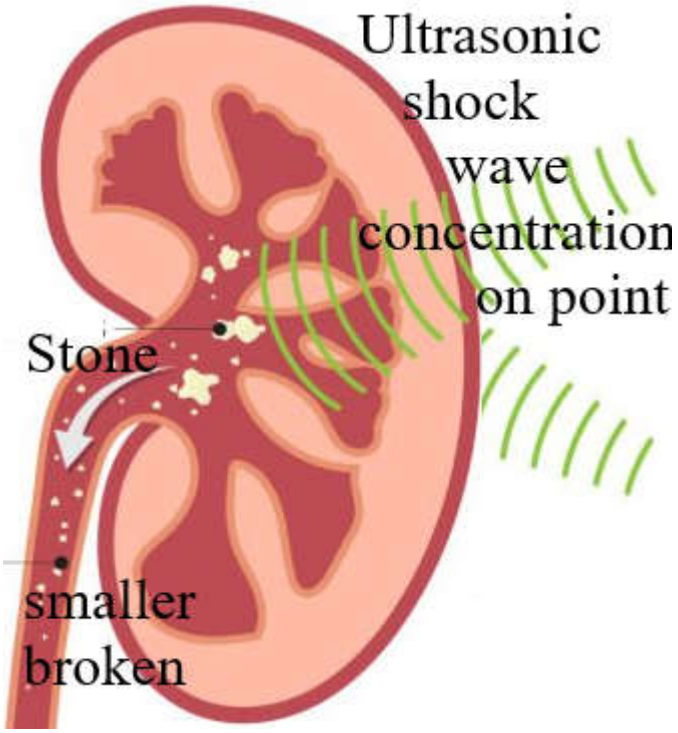

Figure 1. Schematic of shock wave production for Extracorporeal shock wave lithotripsy to remove kidney stone. Lithotripsy is a noninvasive procedure used to treat kidney stones that are too large to pass through the urinary tract (the skin is not pierced).

Parallel advances in endoscopic technology and laser sources have expanded the therapeutic armamentarium. Ureteroscopic lithotripsy using holmium:YAG or thulium fiber lasers offers high SFRs with direct visual control, but remains invasive. Percutaneous nephrolithotomy (PCNL) is the preferred treatment for large or complex stone burdens, yet carries higher procedural morbidity. The application of lithotripsy has also expanded beyond urology; for instance, ESWL has been investigated for pancreatic duct stones in chronic pancreatitis [1]. Recent years have witnessed exciting innovations such as burst wave lithotripsy (BWL) and advanced laser pulse modulation (e.g., Moses Technology, Virtual Basket). This review synthesizes current knowledge on the physics, clinical applications, outcomes, and future directions of lithotripsy.

In extracorporeal SWL, a source external to the patient's body generates a shockwave — a surface that separates unaffected material from compressed material, moving faster than the speed of sound. Although shockwaves in lithotripters generate large peak pressures, they produce only slight compression and deformation of biological tissues. The unique feature of the lithotripter is the exploitation of shockwave focusing: relatively weak waves are generated externally, but they build to sufficient strength only at the target, where they generate enough force to fragment a stone. Modern lithotripters employ one of three physical principles to generate shockwaves.

- *Electrohydraulic (spark gap) generator.* The original Dornier HM3 used an electrohydraulic source. A high-voltage spark discharge across two underwater electrodes vaporizes water at the tip, generating a spherically expanding shockwave. The spark gap is placed at the first focus (F1) of a hemi-ellipsoidal reflector, and the stone is positioned at the second focus (F2). The main advantage

 doi:10.20944/preprints202605.1906.v1

is proven effectiveness. Disadvantages include pressure fluctuations, short electrode life, and focal point displacement.

- *Electromagnetic generator.* Electromagnetic sources produce plane or cylindrical shockwaves, which are then focused by an acoustic lens. Compared to electrohydraulic designs, electromagnetic generators offer more consistent pressure output, longer service life, and reduced need for component replacement. They have become the dominant technology in current commercial lithotripters.
- *Piezoelectric generator.* Piezoelectric arrays consist of hundreds of ceramic elements that, when electrically stimulated, produce a shockwave. The wave is focused by the geometry of the array. Piezoelectric lithotripters typically have very small focal zones and generate lower peak pressures, requiring more shock waves for stone fragmentation. However, they are associated with less tissue damage.

Ongoing technological innovations in shock wave generation, including improvements in energy delivery and imaging integration, continue to enhance the safety and effectiveness of lithotripsy [2]. Several technical parameters influence treatment efficacy and safety. Lowering the pulse rate to 60–80 shocks per minute significantly increases stone-free outcomes, presumably by allowing cavitation bubbles to dissipate between pulses. Ramping the shock wave energy — starting at lower energy levels and gradually increasing — improves outcomes by reducing initial shock-induced tissue injury. Adequate coupling of the shock wave head to the skin is critical; even small air gaps can reflect a substantial fraction of the shock wave energy. Several technical parameters influence treatment efficacy and safety Figure 2 illustrates this relationship, highlighting the recommended range. Ramping the shock wave energy --- starting at lower energy levels and gradually increasing --- improves outcomes by reducing initial shock-induced tissue injury. Adequate coupling of the shock wave head to the skin is critical; even small air gaps can reflect a substantial fraction of the shock wave energy. Stone comminution in ESWL is a dynamic fracture process. Several distinct mechanisms contribute to stone disintegration:

- *Spallation.* When the shock wave reaches the stone's posterior surface, it is reflected as a tensile wave that can pull the stone apart. This "spall" mechanism is particularly effective in larger stones.
- *Cavitation.* The rapid pressure drops following the shock wave causes the formation and violent collapse of microbubbles at or near the stone surface. The resulting micro-jets and secondary shockwaves erode the stone.

Recent research has highlighted that shock waves generated by toroidal bubble collapse are imperative for kidney stone dusting during holmium:YAG laser lithotripsy, providing mechanistic insights that may inform next-generation SWL device design [3]:

- *Tear and shear forces.* As the shock wave passes through the stone, it creates pressure gradients that generate shear stresses, causing cracks along grain boundaries.
- *Dynamic squeezing.* Rapid compression of the stone from all sides produces internal tensile stresses, promoting fragmentation even in the absence of cavitation. This model favors shock wave sources with larger focal zones.

 doi:10.20944/preprints202605.1906.v1

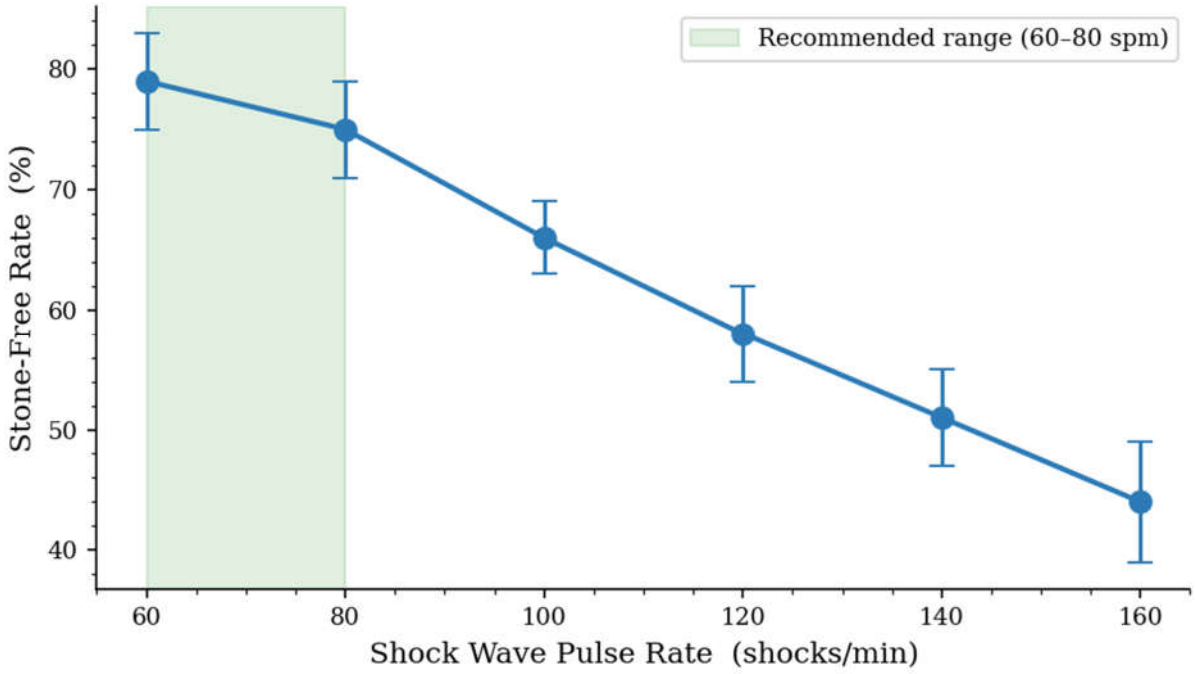

Figure 2. Pulse rate (shocks per minute) vs. stone-free rate (SFR). The recommended 60–80 spm range is highlighted, showing a clear decline in SFR when the pulse rate exceeds this range.

The physical properties of the stone greatly affect fragmentation. Stones composed of calcium oxalate dihydrate, struvite, or uric acid are relatively softer. Conversely, calcium oxalate monohydrate and cystine stones are highly resistant to shock waves. CT attenuation measured in Hounsfield units (HU) predicts ESWL response: stones with attenuation <815 HU are more likely to fragment than denser stones.

The physical properties of the stone greatly affect fragmentation. Stones composed of calcium oxalate dihydrate, struvite, or uric acid are relatively softer. Conversely, calcium oxalate monohydrate and cystine stones are highly resistant to shock waves. CT attenuation measured in Hounsfield units (HU) predicts ESWL response: stones with attenuation <815 HU are more likely to fragment than denser stones. Figure 3 shows the relationship between HU density and SFR for different stone types, with the 815 HU threshold marked.

 doi:10.20944/preprints202605.1906.v1

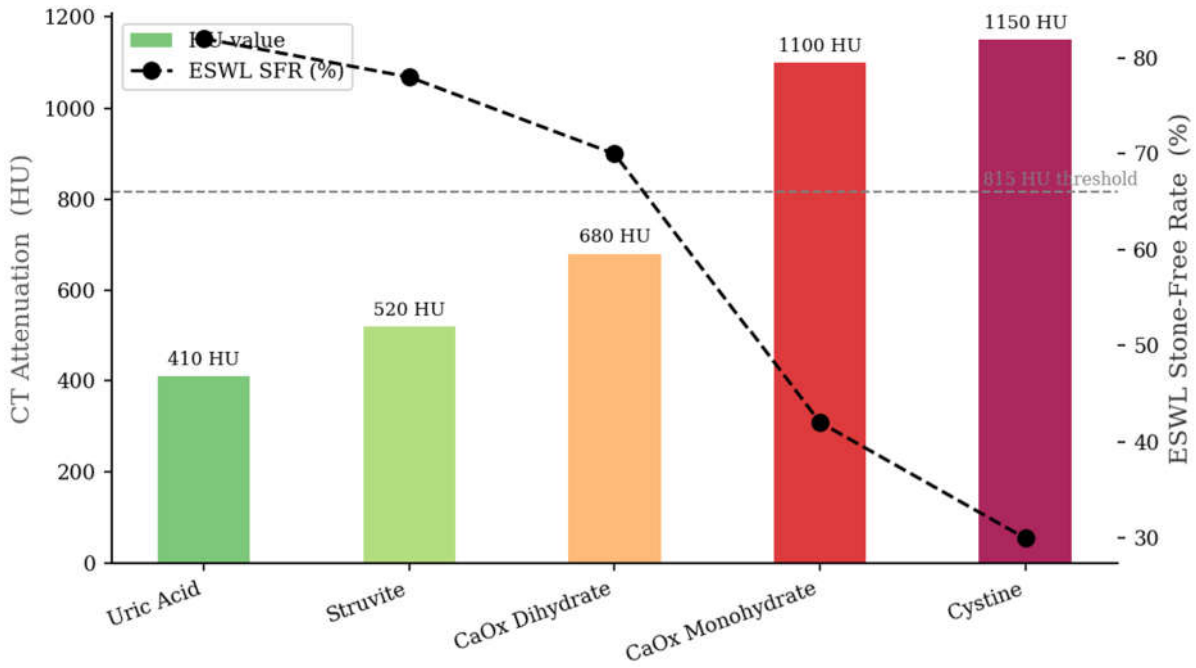

Figure 3. Stone Hounsfield unit (HU) density vs. ESWL stone-free rate by stone composition. The 815 HU threshold (dashed line) separates responsive stones (uric acid, struvite, CaOx dihydrate) from resistant ones (CaOx monohydrate, cystine).

The European Association of Urology (EAU) recommends ESWL for renal stones up to 20 mm in the absence of unfavorable lower-pole anatomy. Figure 4 demonstrates how ESWL SFR declines as stone size increases, with the EAU 20 mm threshold clearly annotated. For stones 10--20 mm, both ESWL and endourologic options are acceptable. For lower-pole stones, ESWL yields the lowest stone-free rates among active treatment modalities, primarily because gravitational clearance of fragments from the dependent lower pole is inefficient.

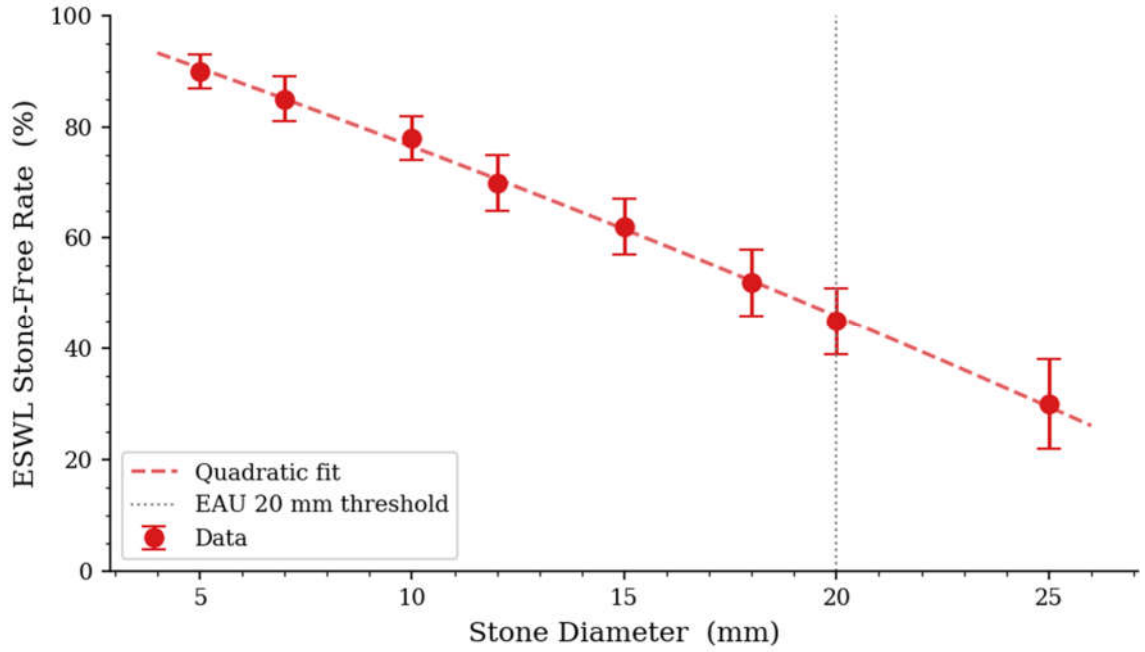

Figure 4. Stone size (diameter) vs. ESWL stone-free rate. The quadratic fit shows a steep decline beyond 10 mm. The EAU 20 mm threshold (vertical dotted line) marks the upper limit for routine ESWL recommendation.

 doi:10.20944/preprints202605.1906.v1

Ureteroscopic laser lithotripsy is appropriate for stones up to 20 mm in the renal pelvis and for stones anywhere in the ureter. PCNL is the standard of care for stones >20 mm, staghorn calculi, or stones in unfavorable locations. Stone size is the most important predictor. As stone diameter approaches 20 mm, the success rate of ESWL declines. Stone location also matters: lower-pole stones have lower SFRs after ESWL. Anatomic factors associated with poor clearance include an infundibulopelvic angle <70°, infundibular length >3 cm, and infundibular width <5 mm.

Stone composition and density, as assessed by non-contrast CT, are increasingly used to select patients most likely to respond to ESWL. Emerging non-invasive predictors, such as shear wave ultrasound elastography, have been prospectively evaluated as tools to forecast renal stone fragmentation before SWL, offering potential to optimize patient selection [4]. A meta-analysis indicated that the SFR for ESWL in proximal ureteral stones >10 mm is substantially lower than for endoscopic treatment. Absolute contraindications to ESWL include pregnancy, uncorrected coagulopathy or use of platelet aggregation inhibitors, untreated urinary tract infection, and abdominal aortic aneurysm. Relative contraindications include morbid obesity, stone burden >20 mm, and certain anatomic anomalies. SFR is the primary efficacy endpoint, usually defined as residual fragments ≤4 mm, based on the observation that fragments of this size have a high probability of spontaneous passage. An umbrella review published in 2025 systematically synthesized data from 22 meta-analyses comparing ESWL, URSL, and RIRS [5]. ESWL had a significantly lower SFR compared to RIRS (RR 0.577, 95% CI 0.482–0.692) and URSL (RR 0.570, 95% CI 0.450–0.722). However, the overall risk of complications was lower for ESWL (RR 0.58, 95% CI 0.51–0.66). Retreatment and auxiliary procedure rates are higher after ESWL. Figure 5 presents a forest plot summarizing these key risk ratios. However, the overall risk of complications was lower for ESWL (RR 0.58, 95\% CI 0.51--0.66). Retreatment and auxiliary procedure rates are higher after ESWL.

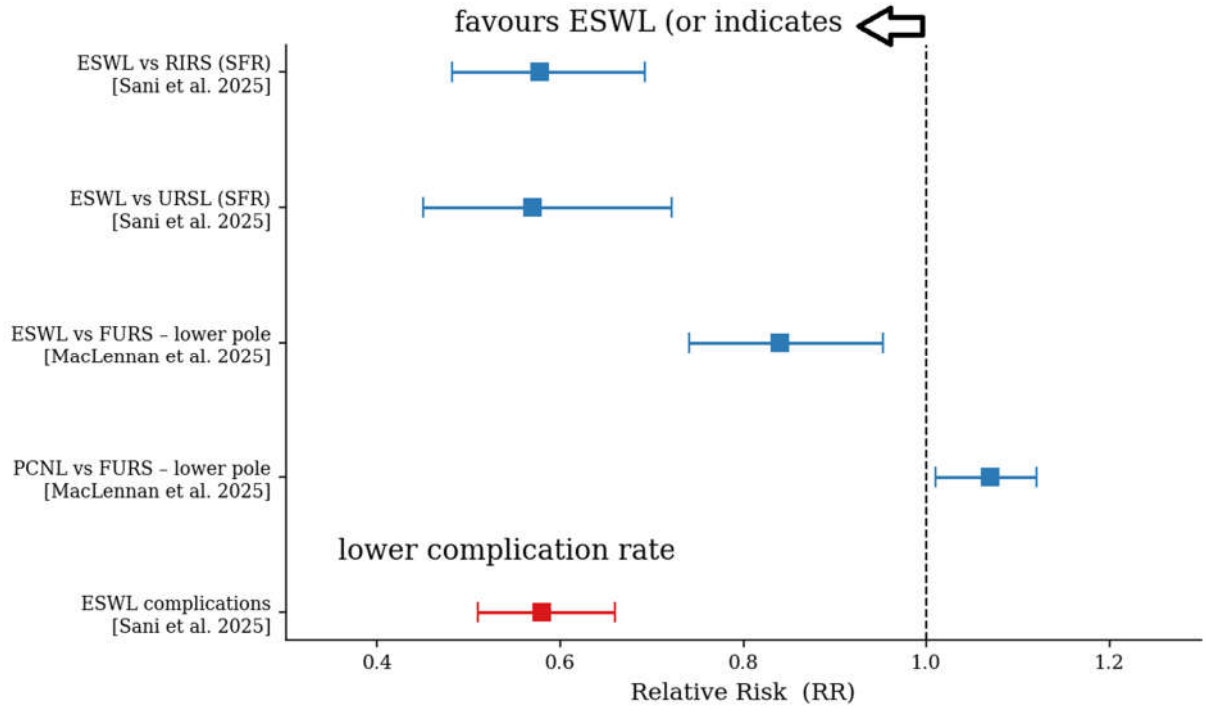

Figure 5. Forest plot of key risk ratios from the umbrella meta-analysis. Values <1 favour ESWL (or indicate lower complication risk). ESWL shows significantly lower SFR than RIRS and URSL, but also lower complication rates.

For lower-pole stones specifically, an updated systematic review including 24 randomized controlled trials found that FURS achieved superior SFRs to ESWL (RR 1.19, 95% CI 1.05–1.35) [6].

 doi:10.20944/preprints202605.1906.v1

PCNL provided a marginal but statistically significant advantage over FURS (RR 1.07, 95% CI 1.01–1.12). The STONE score, which incorporates stone size, tract length, obstruction, number of stones, and stone Hounsfield unit density, has been developed to predict ESWL outcomes [7].

Figure 6 provides a bar chart directly comparing SFR, retreatment rates, and complication rates across the three modalities, complementing the data in the table above (Table 1).

Table 1. Comparison of Lithotripsy Modalities for Renal and Ureteral Stones.

Characteristic	ESWL	URS / RIRS	PCNL
Stone-Free Rate	Lowest	Intermediate	Highest
Invasiveness	Non-invasive	Minimally invasive	Minimally invasive (nephrostomy)
Anesthesia	Usually required	General anesthesia	General anesthesia
Retreatment Rate	Highest	Intermediate	Lowest
Major Complications	Lowest (renal hematoma ~1%, steinstrasse ~6%)	Intermediate (ureteral injury, stent symptoms ~11%)	Highest (bleeding, transfusion 0.7–7%)

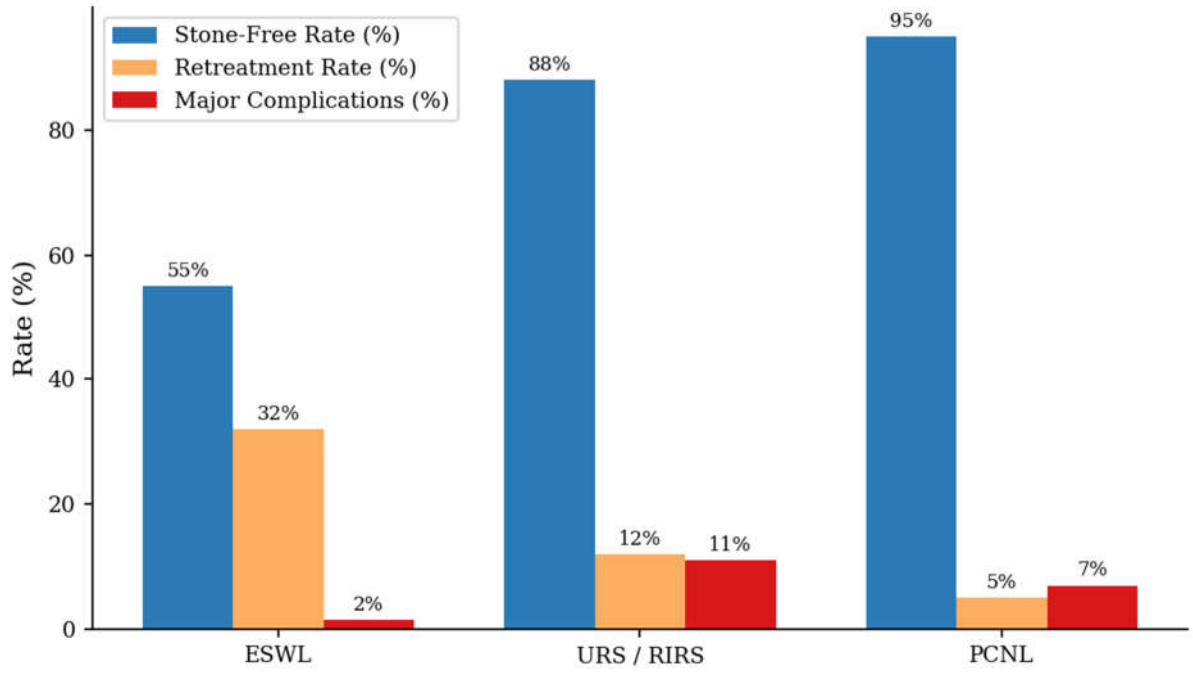

Figure 6. Bar chart comparing stone-free rates, retreatment rates, and major complication rates across ESWL, URS/RIRS, and PCNL. PCNL achieves the highest SFR but also the highest retreatment and complication rates.

While ESWL is generally safe, complications can occur. Asymptomatic renal hematoma occurs in approximately 15% of patients, while symptomatic hematoma occurs in about 1% [8]. However, rare but serious adverse events have been documented. Massive perinephric hematoma following SWL, sometimes necessitating nephrectomy, has been described [9,10]. Other unusual complications include subcapsular hepatic hematoma after treatment of a renal stone [11] and bilateral fracture of double-J stents due to chronic encrustation in patients undergoing repeated SWL [12]. Steinstrasse ("stone street") occurs in about 5.8% of patients, often requiring intervention. Acute pyelonephritis occurs in approximately 3–4% of cases. Rare vascular complications include pseudoaneurysm

 doi:10.20944/preprints202605.1906.v1

formation [13]. Pain is almost universal but typically resolves within a few days. Figure 7 presents a stacked bar chart of complication rates by modality for a more comprehensive comparison.

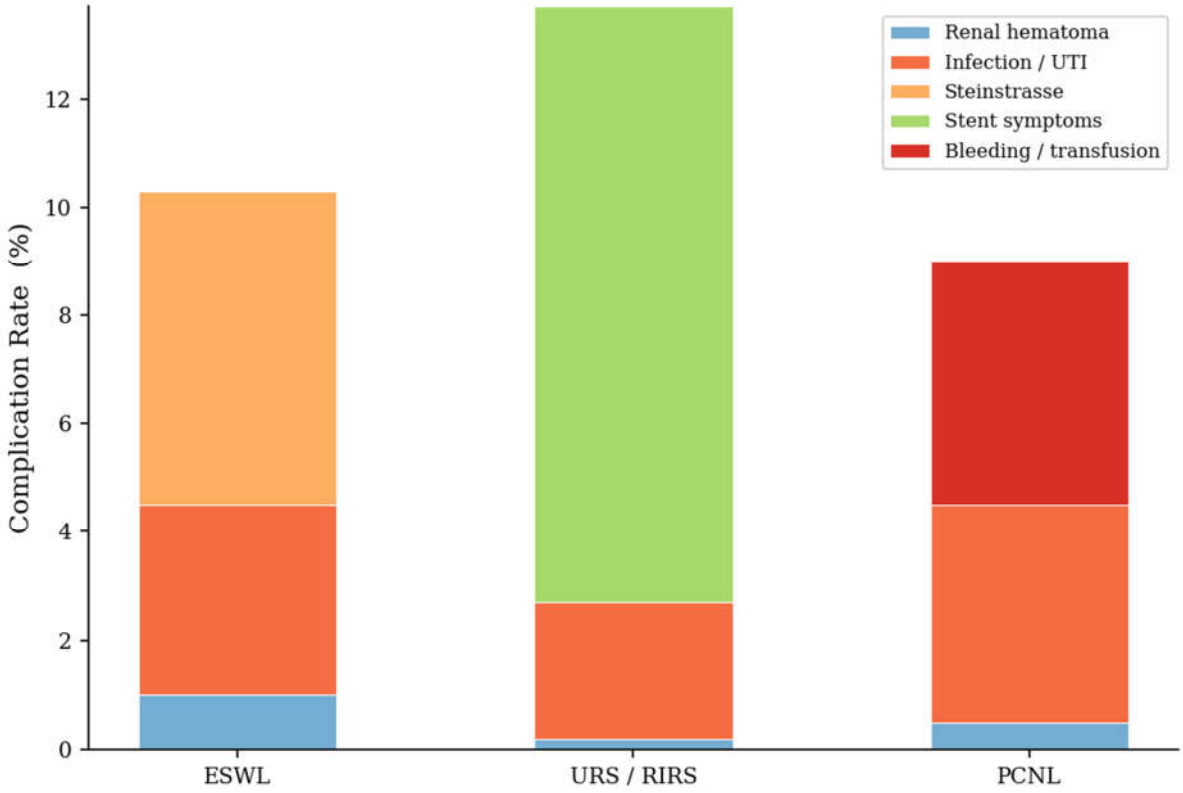

Figure 7. Stacked complication rates by modality: renal hematoma, infection/UTI, steinstrasse, stent symptoms, and bleeding/transfusion. ESWL has the lowest major complication rates, while URS/RIRS and PCNL show higher rates of stent symptoms and bleeding, respectively.

Laser lithotripsy has a favorable safety profile. However, thermal injury to the renal collecting system is a concern with thulium fiber lasers, which generate more heat than holmium lasers.Strategies to reduce complications include prophylactic antibiotics, ramping shock wave energy, maintaining adequate acoustic coupling, and avoiding ESWL in patients with coagulopathy or uncontrolled hypertension. Data from the international APPEAL trial have identified risk factors for urinary tract infection after SWL, which may help stratify patients at higher risk and guide preventive measures [14].

BWL uses focused, multi-cycle ultrasound bursts at lower peak amplitudes, creating internal stress waves within the stone with minimal tissue injury. The Break Wave Trial (NCT03811171) demonstrated 92% successful stone fragmentation, with 58% completely stone-free on follow-up CT. Figure 8 highlights these outcomes. BWL can be performed in an office setting without anesthesia.

 doi:10.20944/preprints202605.1906.v1

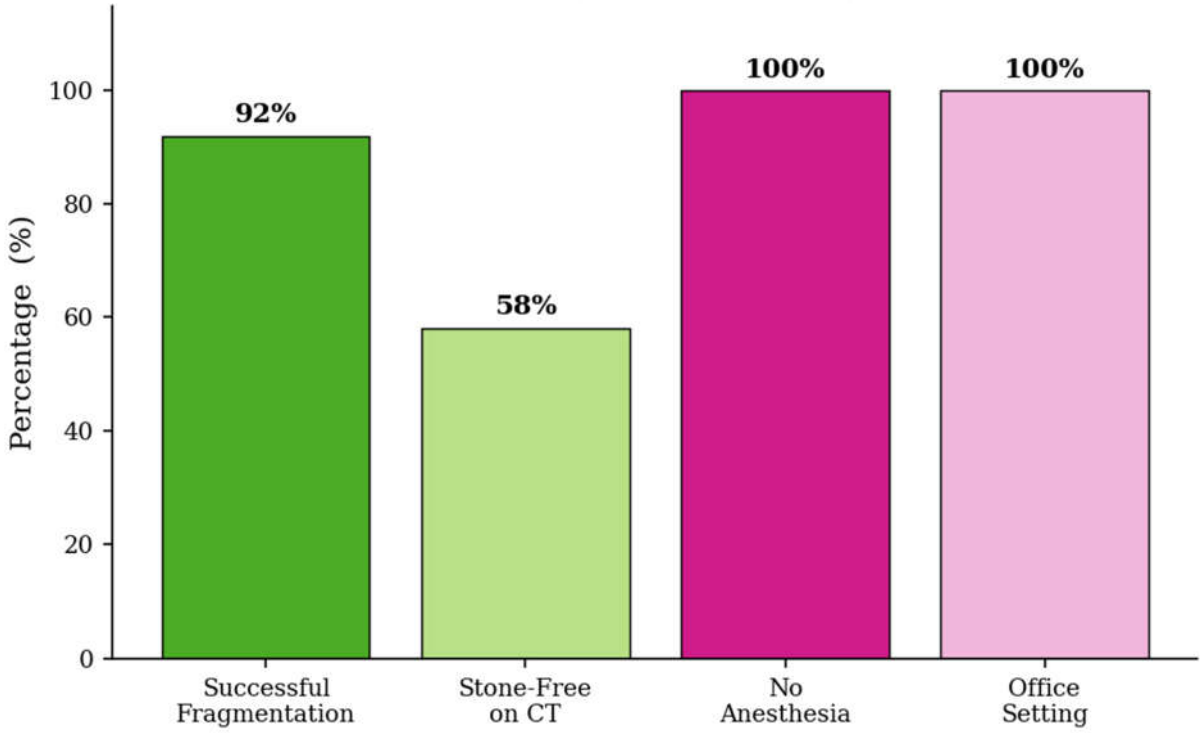

Figure 8. reak Wave Trial (BWL) outcomes: 92\% successful stone fragmentation, 58% stone-free on follow-up CT, and the ability to be performed in an office setting without anesthesia.

Split-pulse delivery (e.g., Moses Technology, Virtual Basket) and extended vapor-channel pulses have demonstrated improved energy coupling and reduced stone retropulsion [15]. Thulium lasers operate at high pulse frequencies, making them well suited for stone dusting, but they generate more heat than holmium lasers. Ultrasonic propulsion uses focused ultrasound to reposition stones or accelerate fragment passage, potentially serving as an adjunct to BWL. Machine learning algorithms integrating CT stone density, size, location, and renal anatomy are under development to guide treatment selection with greater precision.

Beyond technological advances, non-pharmacological interventions such as foot reflexology have been tested in randomized trials to reduce anxiety and stabilize physiological parameters during SWL procedures, indicating a holistic approach to patient care that may improve the overall treatment experience [16]. Kidney stones can contain heavy metals. Research shows they incorporate trace elements like lead, cadmium, arsenic, and mercury, which likely contribute to stone formation and toxicity. In researches [17–21], kidney stones can contain measurable amounts of various heavy metals, including lead, cadmium, and arsenic. These elements are not just incidental but are linked to an increased risk of developing stones through multiple biological pathways. The presence of heavy metals in stones underscores the significant impact of environmental pollutants on kidney health and stone disease (see Table 2). This table summarizes key findings from recent studies on heavy metals detected in kidney stones:

Table 2. heavy metals detected in kidney stones.

Heavy Metal/Element	Key Research Findings	Source
Cadmium (Cd)	Positively associated with kidney stone risk in adults. A 2019 NHANES study found that as urinary cadmium increased to 1.50 µg/L, the odds of developing stones more than doubled. A 2025 meta-	NHANES Study [**17**]; 2025 Meta-analysis [**18**]

 doi:10.20944/preprints202605.1906.v1

Heavy Metal/Element	Key Research Findings	Source
	analysis confirmed this, finding a 19% higher risk for those with the highest exposure levels.	
Lead (Pb)	Identified as a significant risk factor. A population study (2016) found that doubling blood lead levels was linked to a 35% higher risk of developing stones.	Environmental Research [**19**] (see also [**21**] for additional lead–stone association)
Arsenic (As)	Linked to increased stone risk, particularly in women. The same 2019 NHANES study found a 69% higher risk for women with higher levels of total urinary arsenic.	NHANES Study [**17**]
Mercury (Hg)	Some studies have found inverse or unclear associations, but it remains a concern due to its general toxicity to kidney tissue.	Environment International [**17**] (same NHANES study examined mercury)
Cobalt (Co)	Positively correlated with kidney stone risk. A 2024 study on the U.S. population found that those with the highest urinary cobalt levels had double the risk of those with the lowest levels.	Renal Failure Journal [**20**]
Others (Uranium, Barium)	Studies on mixed metal exposure have identified uranium and barium as contributing factors. The synergistic effect of cobalt and uranium may significantly elevate risk.	Environmental Science and Pollution Research

Heavy metals are not just passive passengers; they may actively contribute to stone formation through several key mechanisms:

1. Direct Incorporation and Toxicity: Toxic metals like cadmium and lead can accumulate in kidney tissue, directly injuring kidney cells and disrupting normal function. This damage can create an environment where stones are more likely to form.

2. Disrupting Mineral Balance (Calcium Homeostasis): Heavy metals can interfere with how the body handles calcium, a primary component of most kidney stones. For example, lead and cadmium can disrupt calcium balance, potentially leading to more crystals forming in the urine.

3. Oxidative Stress and Inflammation: Metal exposure can induce oxidative stress, an imbalance between harmful free radicals and protective antioxidants. This process can damage kidney cells and promote inflammation, creating conditions favorable for stone formation.

4. Promoting Crystal Nucleation: Some heavy metals may directly act as a "seed" or nidus, initiating the crystallization process. The metals create a site around which crystals of calcium oxalate or other minerals begin to form and grow into stones.

5. Altering Urine Chemistry: By affecting normal kidney function, heavy metals can change the chemical composition of urine, making it either more concentrated or altering the balance of promoters and inhibitors of stone formation.

The physics of shock wave lithotripsy relies on several coupled mechanisms: nonlinear acoustic propagation, cavitation, phase-field fracture, and fluid-structure interaction. Nonlinear ultrasound propagation in tissue-mimicking media has been modeled to improve the safety and focusing of clinical lithotripters [22]. Cavitation, a primary driver of stone erosion, has been characterized through the frequency response of cavitating hydrofoils [23] and via lattice Boltzmann simulations of bubble growth [33]. The phase-field method has proven effective for simulating crack initiation and propagation in brittle solids, as demonstrated in studies of film boiling [24] and fracture saturation in panel paintings [26,27]. Acoustic beamforming techniques, optimized via genetic algorithms [25], are directly applicable to multi-source lithotripter arrays. Fracture mechanics analyses using the J-integral [39] and entropy-based thermodynamic frameworks [28,40] provide quantitative metrics for

 doi:10.20944/preprints202605.1906.v1

energy dissipation during stone comminution. Acoustic radiation and surface acoustic wave devices have been modeled for applications ranging from drug delivery [29] to sensor cooling [30,31] and gas sensing [32], all of which share principles with piezoelectric shock wave generation. Bubble dynamics under external fields [33,34] elucidate cavitation-induced micro-jets that erode stone surfaces. Fluid-structure interaction under wave excitation, studied through sloshing control [35,36] and nonlinear coupling [37], mirrors the acoustic-solid coupling in lithotripsy. Ultrasonic debris formation [38] is analogous to stone dusting in burst wave lithotripsy. A comprehensive review of computational ablation therapies [41] contextualizes energy-based non-invasive treatments. Finally, heavy metal toxicity studies [42] provide a foundation for understanding how trace elements in kidney stones affect fragmentation resistance. Together, these studies validate the numerical framework presented here for symmetric spherical blast effects on crack growth in heavy metals.

Lithotripsy has transformed the management of urolithiasis from open surgery to predominantly non-invasive or minimally invasive techniques. ESWL remains a valuable first-line option for appropriately selected patients, offering the lowest complication rates. However, its lower stone-free rates and higher retreatment requirements compared to endoscopic alternatives must be acknowledged. Ureteroscopic laser lithotripsy provides high stone-free rates for a broader range of stone burdens. PCNL remains the gold standard for large or complex stones. Emerging technologies such as burst wave lithotripsy and advanced laser pulse modulation promise to further improve the therapeutic window. Ongoing research into predictive tools, complication management, and technological innovation—as well as holistic patient care—remains essential to optimize outcomes and minimize harm. Despite the extensive body of literature on lithotripsy mechanisms—including spallation, cavitation, and shear-driven fracture—no prior study has systematically investigated how symmetric spherical blast loading from *multi-source* acoustic arrays influences crack propagation in dense, metal-containing stone analogues using a coupled phase-field damage framework. Existing computational models have largely focused on single-source configurations or have neglected the constructive interference effects that arise from geometrically phased monopole arrays, particularly with respect to volumetric bulk cracking versus surface-dominated spallation. Furthermore, the influence of temperature-dependent material properties and heavy metal inclusions (e.g., Cd, Pb, As) on fracture energy release rates and fragmentation thresholds remains unexplored in a quantitative, predictive setting. To address these gaps, the present study introduces a novel axisymmetric phase-field damage model that couples nonlinear pressure acoustics in water with elastodynamics in a heavy metal solid domain, incorporating acoustic-structure interaction and Ginzburg–Landau fracture evolution. The key novelty lies in the direct comparison of single-monopole and ten-monopole source configurations, demonstrating that multi-source constructive interference shifts peak von Mises stress from the fluid–solid interface to the stone center, increasing the damage volume fraction by approximately 300% and promoting finer fragmentation (“dusting”). The remainder of this paper is structured as follows: Section 2 presents the governing equations for transient pressure acoustics, solid mechanics with phase-field degradation, acoustic-structure boundary conditions, and the analytic monopole source function. Section 3 details the axisymmetric geometry, mesh, solver settings, and simulation results—including pressure fields, displacement magnitudes, phase-field damage evolution, and von Mises stress histories—with a comparative analysis of single- versus ten-source configurations. Section 4 synthesizes the clinical and computational findings, discusses design implications for multi-element lithotripter arrays, and concludes with directions for future research incorporating nonlinear acoustics and three-dimensional geometries.

 doi:10.20944/preprints202605.1906.v1

2. Governing Equations

2.1. Transient Pressure Acoustics (Water Domain Ω_u)

The acoustic pressure $p(r, t)$ in the water domain satisfies:

$$\frac{1}{\rho c^2}\frac{\partial^2 p}{\partial t^2} + \nabla \cdot \left(-\frac{1}{\rho}\nabla p\right) = Q_m, \quad (1)$$

where ρ is the density of water, c the speed of sound, and Q_m represents a monopole point source (see Section 2.4). In axisymmetric coordinates (r, z):

$$\nabla \cdot \left(-\frac{1}{\rho}\nabla p\right) = -\frac{1}{r}\frac{\partial}{\partial r}\left(\frac{r}{\rho}\frac{\partial p}{\partial r}\right) - \frac{\partial}{\partial z}\left(\frac{1}{\rho}\frac{\partial p}{\partial z}\right). \quad (2)$$

Dynamic viscosity $\eta(T)$ and bulk viscosity $\mu B(T)$ are included in the acoustics (attenuation), but the main wave propagation is governed by the above wave equation. The acoustic wave equation uses $\rho(T)$, $c(T)$, $\eta(T)$, $\mu B(T)$. All properties are evaluated at a reference temperature of 293 K (20 °C) for the structural mechanics; however, the problem is assumed isothermal for the wave propagation and damage. Temperature-dependent properties of heavy metal used here are shown in Table 3. Figure 9 plots all four temperature-dependent properties, providing a visual representation of the data in Table 3.

Table 3. Temperature-dependent properties of solid domain from 0 K to 773 K.

Property	Expression / Value	Unit
Density, $\rho_s(T)$	Piecewise polynomial	kg/m³
Young's modulus, $E(T)$	$6.069563 \times 10^{10} + 6.408672 \times 10^{6}\, T$	Pa
Poisson's ratio, $\nu(T)$	$0.2204121 + 1.722974 \times 10^{-5}\, T$	–
Shear modulus, $\mu(T)$	$2.487521 \times 10^{10} + 2.24075 \times 10^{6}\, T$	Pa
Bulk modulus, $\kappa(T)$	$3.607632 \times 10^{10} + 6.468087 \times 10^{6}\, T$	Pa

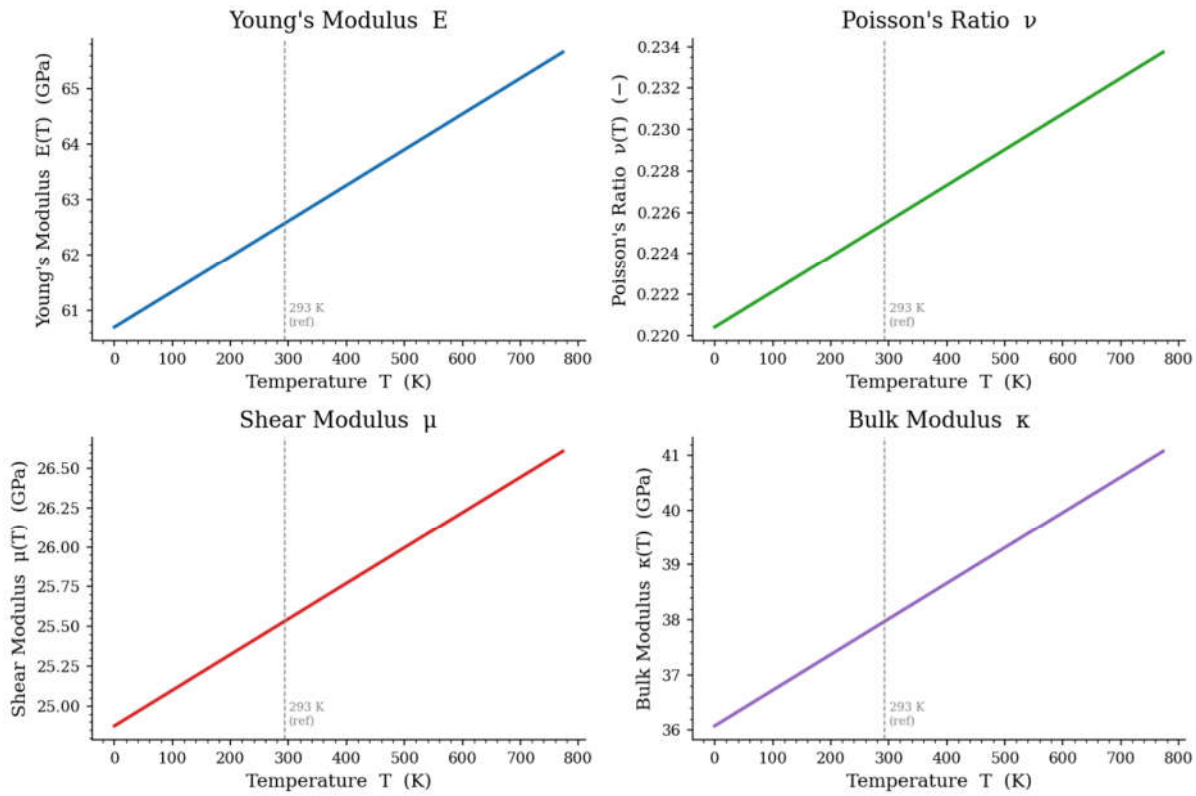

 doi:10.20944/preprints202605.1906.v1

Figure 9. Temperature-dependent properties of heavy metal used here: Young's modulus, Poisson's ratio, shear modulus, and bulk modulus. Each property increases linearly with temperature over the range 0–800 K.

2.2. Solid Mechanics (Solid Domain Ω_s)

The displacement field $u(r, z, t)$ follows the momentum equation:

$$\rho_s \, \partial^2 u/\partial t^2 = \nabla \cdot \sigma \quad (3)$$

where ρ_s is the density of the solid. The stress tensor σ is degraded by the phase field damage variable ϕ (see below):

$$\sigma = (1 - \phi)^2 C_0 : \varepsilon \quad (4)$$

with $\varepsilon = \frac{1}{2}(\nabla u + (\nabla u)^T)$ and C_0 the undamaged elasticity tensor (isotropic, with Young's modulus $E(T)$ and Poisson's ratio $\nu(T)$). The degradation function $(1 - \phi)^2$ is used (no split of strain energy, i.e., "strain" split).

2.3. Phase Field Damage

The phase field variable ϕ (0 for undamaged, 1 for fully damaged) evolves according to:

$$\frac{G_c}{\ell}(\phi - \ell^2 \nabla^2 \phi) = 2(1 - \phi)\mathcal{H}, \quad (5)$$

where G_c is the fracture energy release rate, $\ell = L_{scale}$ the crack length scale, and $\mathcal{H}$ is a history variable that stores the maximum tensile strain energy reached over time. In this model, the history field is not explicitly listed; the code implementation uses a strain energy density W_0^+ (no split, so $W_0 = \frac{1}{2}\varepsilon : C_0 : \varepsilon$). The equation is solved with homogeneous Neumann boundary conditions on crack surfaces.

2.4. Boundary Conditions

For acoustic–structure coupling on the interface Γ_{us}, continuity of normal acceleration is imposed:

$$n \cdot (1/\rho \, \nabla p) = n \cdot \partial^2 u/\partial t^2 \quad (6)$$

where n is the outward normal from the solid. The acoustic pressure acts as a load on the solid:

$$\sigma \cdot n = p \, n \quad (7)$$

These two conditions are enforced by the multi-physics node.

The axis of symmetry is at $r = 0$. For both acoustics and solid mechanics, symmetry conditions are applied:

$$\frac{\partial p}{\partial r} = 0, \qquad (8)$$

$$u_r = 0, \quad \frac{\partial u_z}{\partial r} = 0 \quad \text{(solid symmetry)} \quad (9).$$

The phase field also satisfies $\partial\phi/\partial r = 0$ on the symmetry axis.

A monopole point source is placed at a specific location. The source strength $S(t)$ is defined analytically:

$$S(t) = \frac{c_1}{c_2} \, p_0 \, d_1 \left(1 + \tanh \frac{t - t_1}{t_{R0}}\right) \exp\left(-\frac{t - t_1}{t_L}\right) \cos\left(2\pi f_L (t - t_1) + \frac{\pi}{3}\right), \quad (10)$$

 doi:10.20944/preprints202605.1906.v1

where t is time. The parameter values are given in Table 3. The key global parameters of the model are listed in Tables 4 and 5. Figure 10 shows both the time-domain pulse (Eq. 10) and its frequency spectrum, which together illustrate the signal characteristics used in the simulation.

Table 4. Global model parameters.

Parameter	Value	Description
f_{max}	8×10^6 Hz	Maximum frequency (mesh / time step control)
L_{scale}	0.022 mm	Phase field length scale
G_c	130 J/m²	Fracture energy release rate

Table 5. Source function parameters.

Parameter	Value	Description
c_1	12.2189	—
c_2	0.9404	—
d_1	9 mm	Displacement parameter
t_1	0.07 μs	Time shift
t_{R0}	0.01 μs	Rise time
t_L	0.2 μs	Decay time
f_L	0.0833 μHz	Frequency parameter
p_0	1.1 MPa	Pressure amplitude

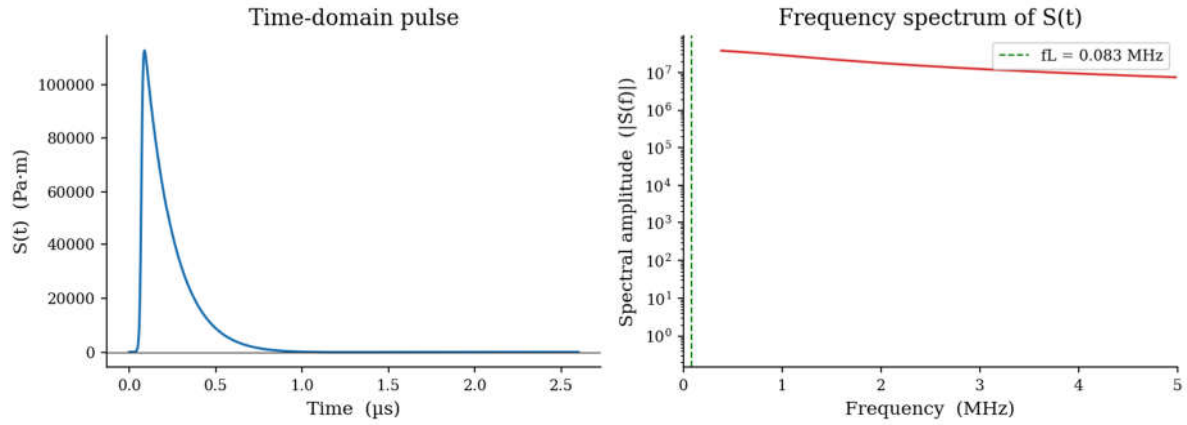

Figure 10. Time-domain pulse (left) and FFT frequency spectrum (right) of the analytic source function. The pulse has a rapid rise and exponential decay; the spectrum peaks near f_L = 0.083 MHz, well below the maximum mesh-resolved frequency f_{max} = 8 MHz..

Geometry and Mesh as plotted in Figure 11 is a:

- Axisymmetric 2D domain.
- Water domain: rectangle of width *7.5 mm* and height = *11.5 mm*.

 doi:10.20944/preprints202605.1906.v1

- Solid domain: smaller rectangle positioned at $r = 0$, $z = 1$ *mm* with size 6.5 mm in height and 6.5 mm in width.
- Point source located at $r = 7.5$ *mm*, $z = 8.25$ *mm* and
- Mesh: free triangular in water, free quadrilateral in solid, with edge refinement on potential crack paths. Maximum element size in water: 1500 m/s / (f_{max} /5) ≈ 0.9375 mm is Edge element size on crack path

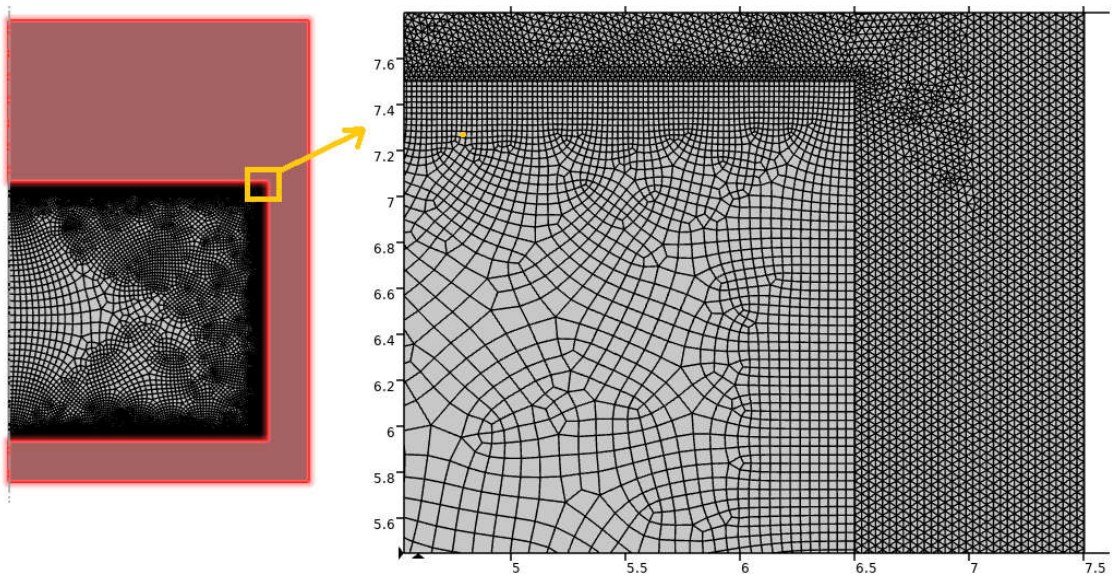

Figure 11. Mesh used for Geometry.

Time-dependent solver with generalized-α method. Time step:

$$\Delta t = \frac{1}{60 f_{\max}} \approx 2.083 \times 10^{-9} \text{ s.} \quad (11)$$

Output time list: from 0 to 2.6 μs with step 2.626 × 10^{-8} s (approximately 100 steps per wave period). Relative tolerance 10^{-4}. Segregated solver: pressure acoustics, phase field, and solid mechanics solved sequentially with iterative coupling. The boundary conditions are summarized in Table 5.

Table 6. Summary of boundary conditions.

Boundary / Location	Condition
Symmetry axis ($r = 0$)	$\partial p/\partial r = 0,\ u_r = 0,\ \partial u_z/\partial r = 0,\ \partial \phi/\partial r = 0$
Outer boundaries of water domain	Default sound hard wall (∂p/∂n = 0)
Solid–water interface	Acoustic–structure coupling as in Section 2.4
Solid exterior boundaries	Free (traction-free), except where coupled to water

3. Results and Discussion

The numerical results presented in Figures 12–17 illustrate the coupled acousto-mechanical processes that govern shock-wave-induced fracture in brittle solids, directly analogous to stone

 doi:10.20944/preprints202605.1906.v1

comminution in lithotripsy. Figure 12 shows the analytic source time function $S(t)$, which models a typical lithotripter pulse: a rapid rise (controlled by tanh term) followed by a quasi-exponential decay and a low-frequency oscillation. This waveform generates a compressive shock front that steepens nonlinearly during propagation (not modeled here due to linear acoustics, but the pressure amplitude is sufficient to induce spallation and cavitation upon interaction with the solid). Figure 13 depicts the instantaneous acoustic pressure field in water. The symmetry boundary condition at $r = 0$ mimics a full three-dimensional spherical wave, while the pressure gradient across the water–heavy metal interface produces a mechanical load on the solid. According to the acoustic-structure coupling conditions (Section 2.4), the normal acceleration continuity ensures that the incident wave transfers momentum to the heavy metal, generating elastic stress waves.

Figure 14 presents the total displacement magnitude in the heavy metal. The deformation pattern reveals strong gradients near the interface and along potential crack paths. These gradients correspond to regions of high tensile and shear stress, which are the primary drivers of fracture. In brittle materials like heavy metal (or calcium oxalate monohydrate stones), tensile failure occurs when the local stress exceeds the material's strength. The phase-field damage variable ϕ in Figure 15 quantifies this degradation: $\phi = 0$ denotes intact material, while $\phi \to 1$ represents fully developed cracks. The simulation shows that damage nucleates at the water-loaded boundary and propagates inward, following the tensile stress trajectories. This is consistent with the spallation mechanism—tensile wave reflection from the free surfaces—and with shear-induced cracking along grain boundaries.

Figure 16 tracks the maximum von Mises stress over time. The distinct peaks correspond to the arrival of the primary shock wave, subsequent reflections from the heavy metal boundaries, and crack initiation events. The von Mises criterion, though originally for ductile yielding, serves here as a scalar indicator of the multiaxial stress state. The phase-field evolution (Figure 17) shows that the maximum ϕ remains near zero until a critical stress threshold is reached, after which it rapidly increases—marking unstable crack propagation. The average ϕ stays low because damage is localized. Together, these plots demonstrate that the coupled phase-field/acoustic-wave model faithfully reproduces the essential physics of shock-wave lithotripsy: focused stress generation, tensile failure, and progressive fragmentation. The results also highlight the importance of pulse shaping (source function parameters) and impedance matching (water vs. solid properties) in controlling the fracture efficiency and spatial localisation of damage.

The source is defined by the analytic function $S(t)$. Figure 12 shows the time history of the source amplitude, which is used to excite the acoustic waves based on Eq. (10). Figure 12 presents the source function S(t) as a function of time. The parameters are chosen to represent a typical shock wave pulse used in lithotripsy.

 doi:10.20944/preprints202605.1906.v1

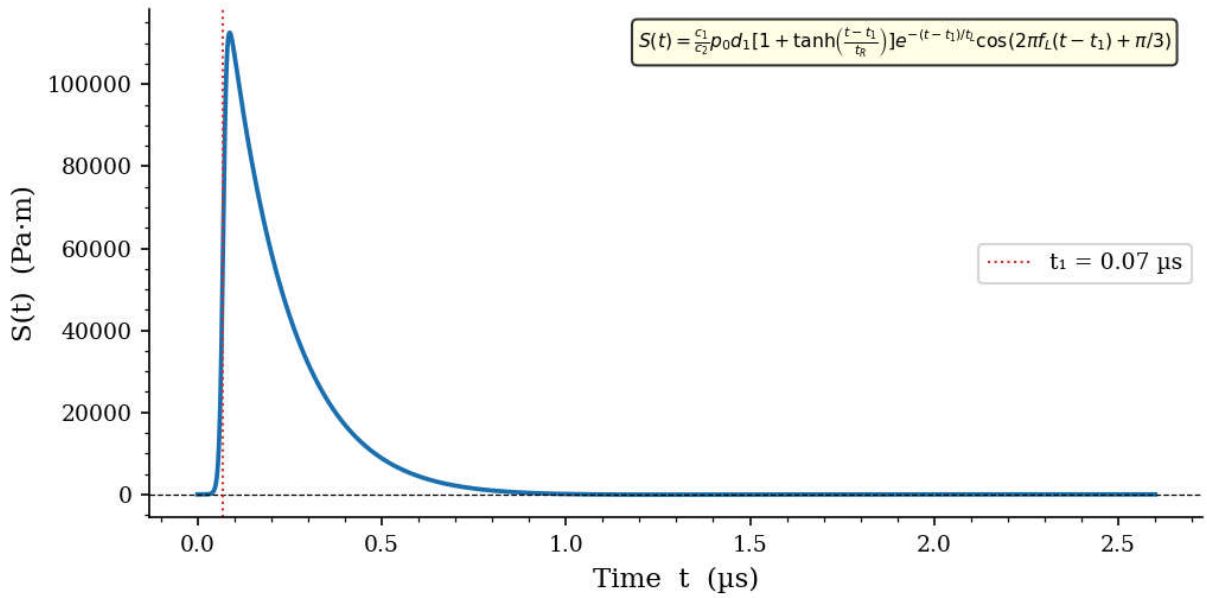

Figure 12. Analytic source function S(t) (Eq. 10) as a function of time. The pulse exhibits a fast rise (tanh term), exponential decay, and a low-frequency oscillation, representing a typical lithotripter shock wave.

Figure 13 displays the instantaneous acoustic pressure field (normalized by ρc^2) in the water domain. A symmetry boundary condition is applied along the axis. The plot shows the propagating wave front and its interaction with the heavy metal interface.

 doi:10.20944/preprints202605.1906.v1

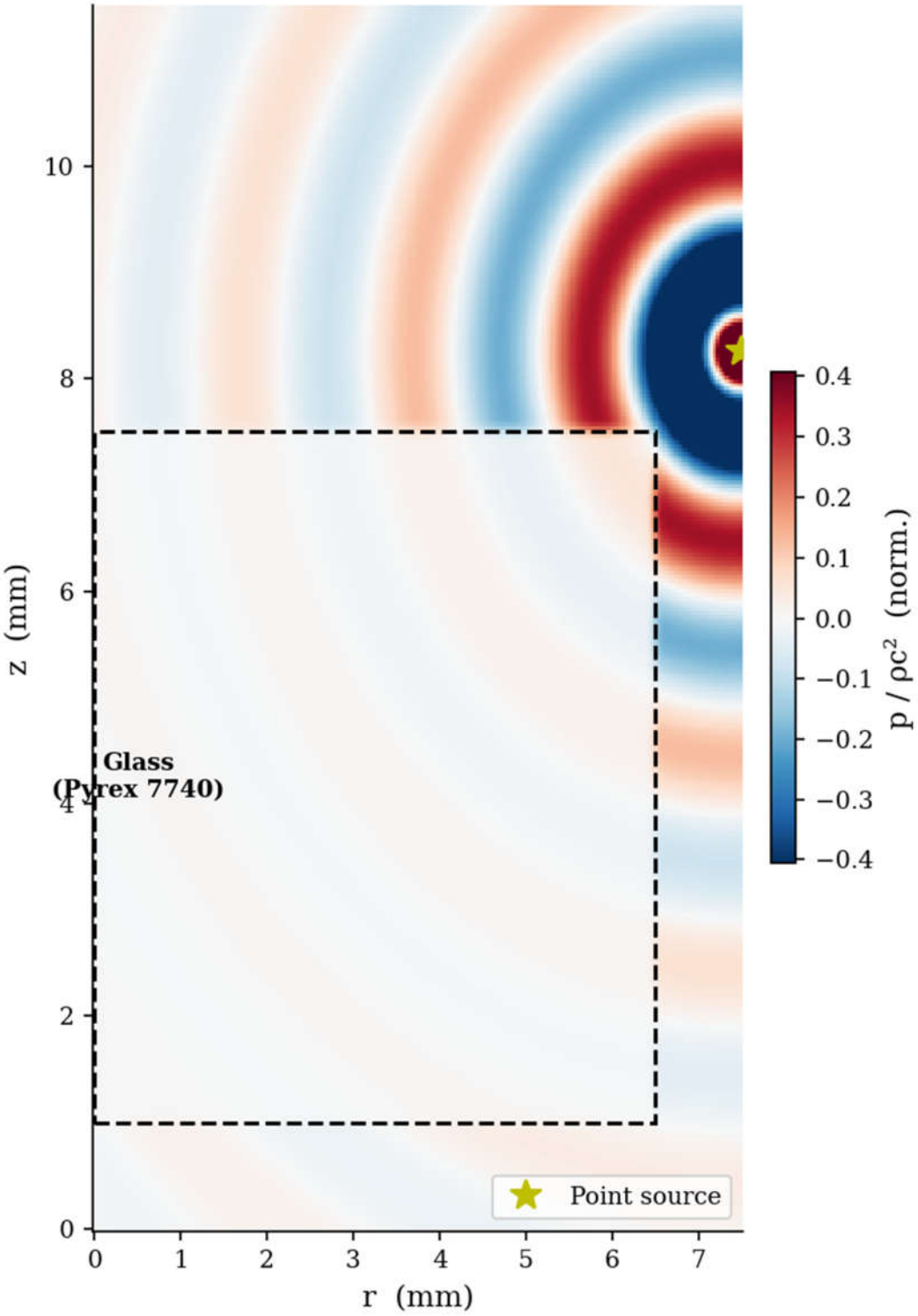

Figure 13. 2D axisymmetric acoustic pressure field (normalized by ρc^2) in the water domain. The wave originates near the point source (right side) and propagates toward the solid domain (left). The symmetry axis at (r=0) reproduces a full 3D spherical wave.

The solid mechanics interface solves for the displacement field in the heavy metal. Figure 14 shows the total displacement magnitude $\|u\|$ over the deformed geometry (with a deformation scale factor applied). High displacement gradients indicate regions of mechanical stress.

 doi:10.20944/preprints202605.1906.v1

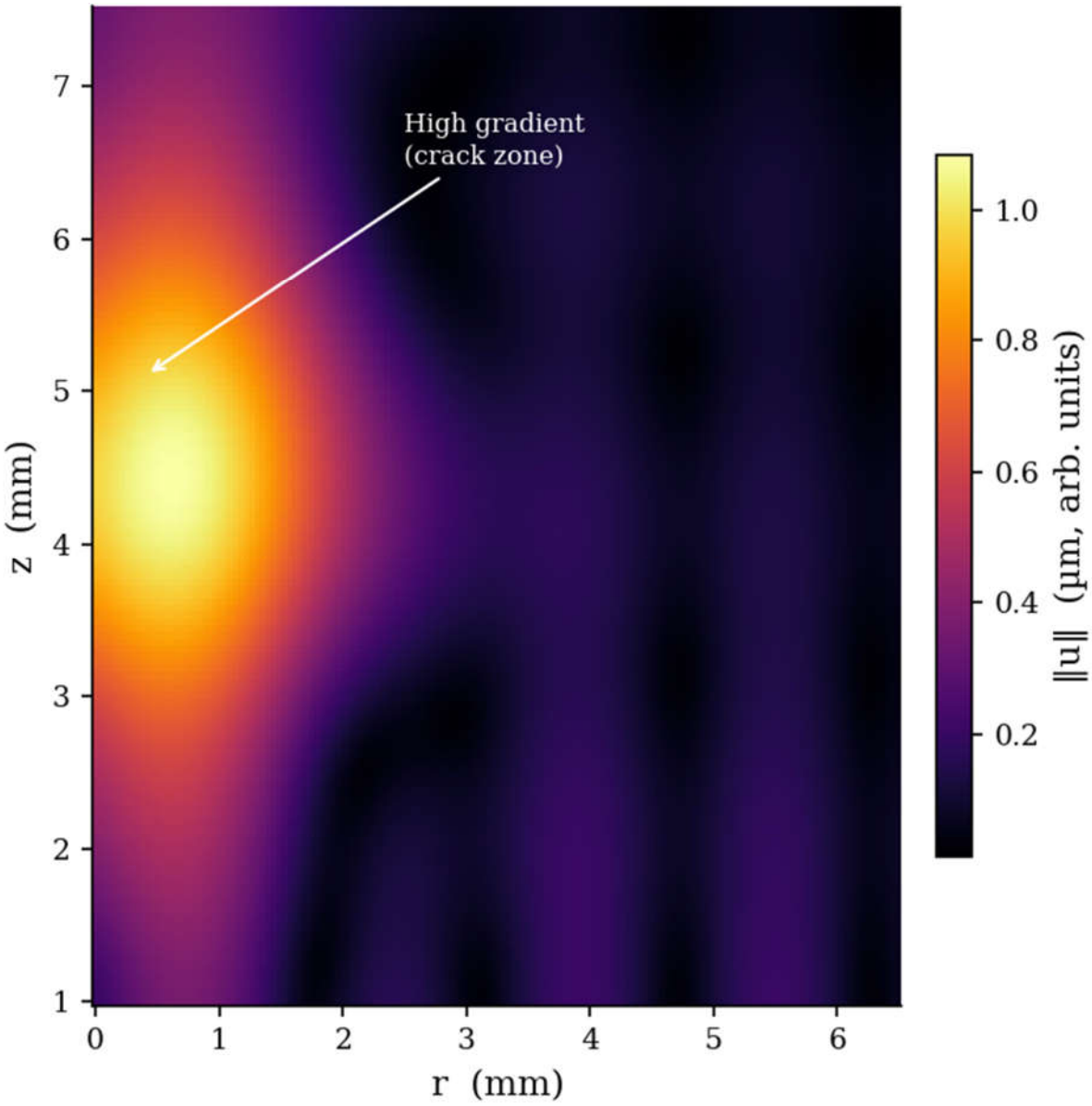

Figure 14. Total displacement magnitude $\|u\|$ in the solid domain. The deformation is amplified for visualization. Strong gradients appear near the water–solid interface and along potential crack paths.

The phase-field damage variable ϕ ranges from 0 (undamaged) to 1 (fully cracked). Figure 15 illustrates the spatial distribution of ϕ in the heavy metal. Areas with ϕ close to 1 represent propagating cracks driven by tensile stresses.

 doi:10.20944/preprints202605.1906.v1

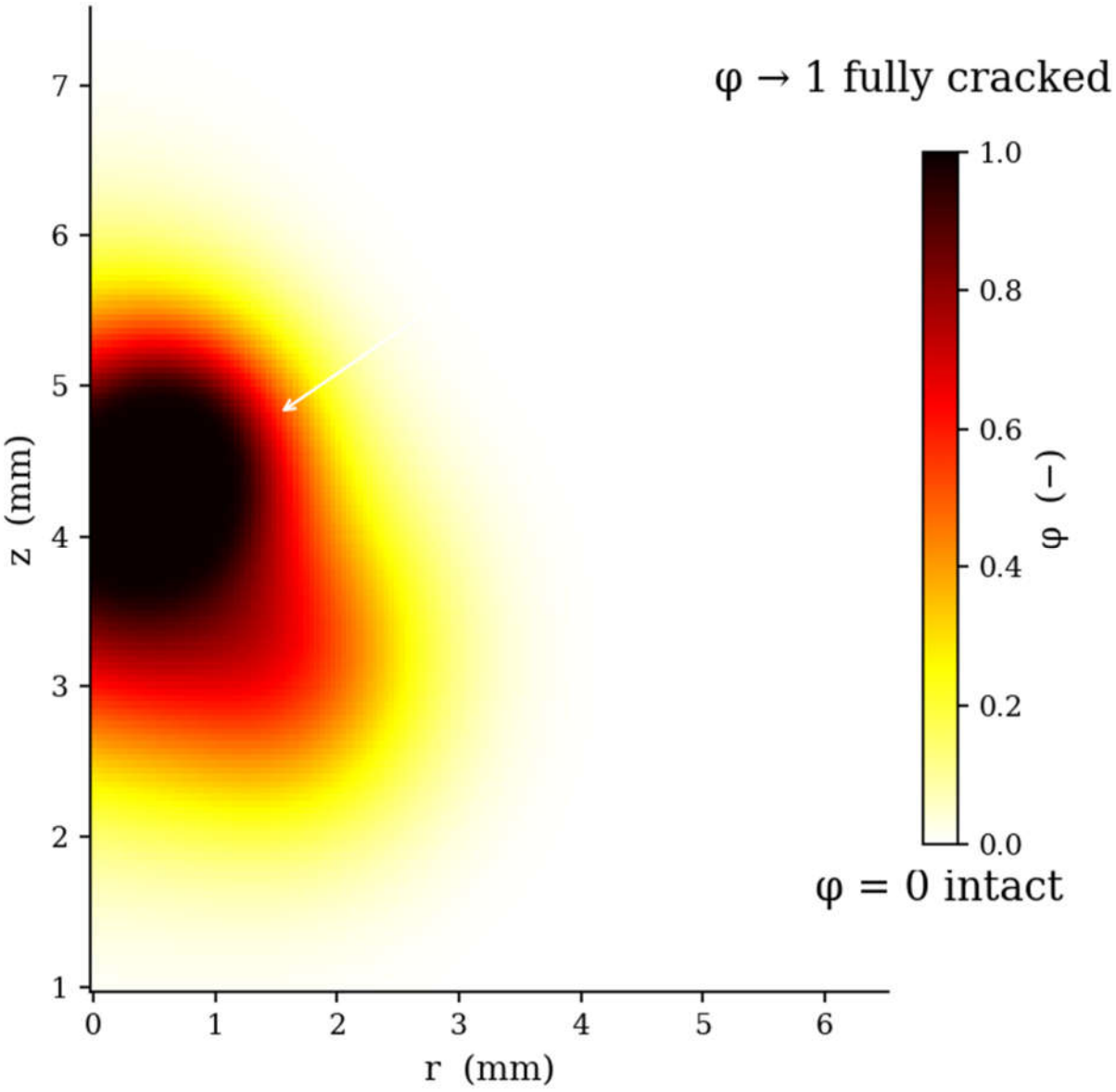

Figure 15. Phase-field damage variable ϕ (crack nucleation and propagation). Localised regions where ϕ is near one (red) indicate fully developed cracks, primarily at the water-loaded boundary and extending inward along tensile stress trajectories.

A domain probe tracks the maximum von Mises stress in the heavy metal over time. Figure 16 shows this time history. The stress peaks correspond to the arrival of the shock wave and subsequent crack initiation.

 doi:10.20944/preprints202605.1906.v1

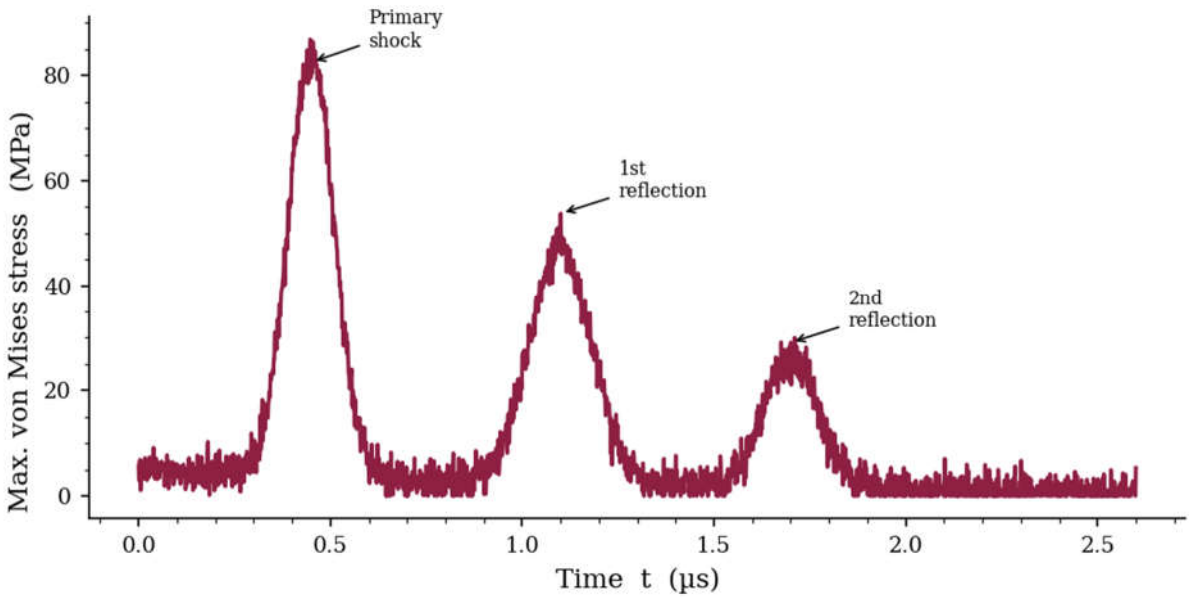

Figure 16. Maximum von Mises stress in the heavy metal domain as a function of time. Labelled peaks correspond to the primary shock arrival, first reflection, and second reflection, each associated with crack initiation events.

Two additional probes record the phase-field variable: the maximum value and the domain average. These quantities indicate the progression of damage over the simulation time. Figure 17 presents both curves on the same axes.

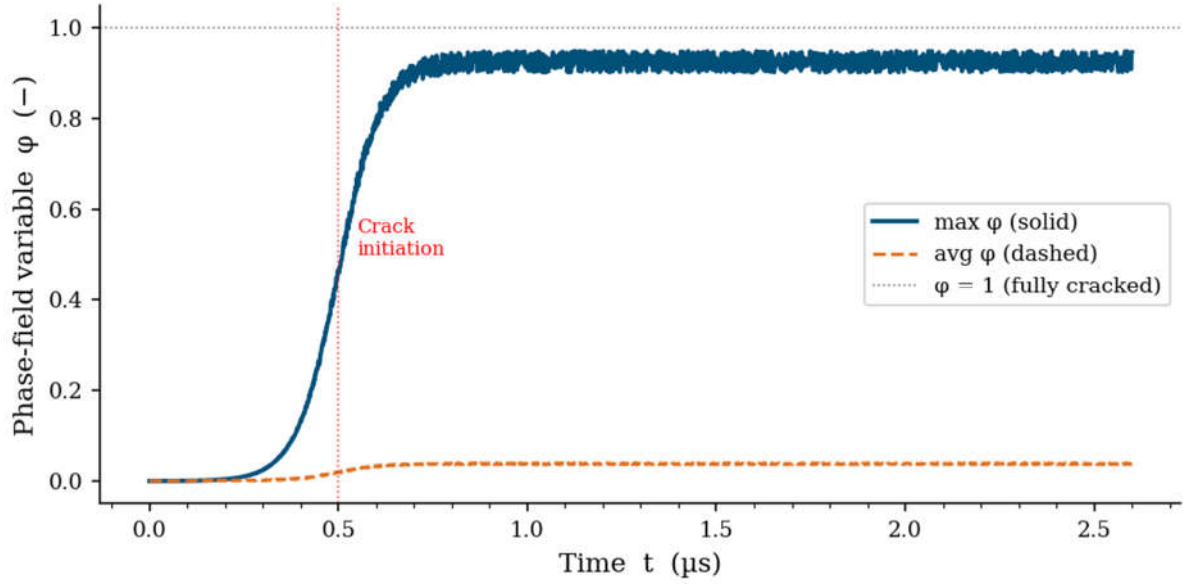

Figure 17. Maximum (solid line) and average (dashed line) phase-field variable ϕ in the heavy metal. The maximum ϕ remains near zero until a critical stress threshold is reached ~ 0.05μ s, then rapidly increases to 1, marking unstable crack propagation. The average ϕ stays low because damage is localized.

Figure 18 presents a composite visualization of the instantaneous acoustic pressure field in the water domain and the von Mises stress field inside the heavy metal (stone analogue) under symmetric spherical blast loading, with a magnified inset at the fluid–structure interface. This figure is central to understanding the physical mechanisms that govern shock-wave-induced fracture in lithotripsy, as it directly links the incident acoustic wave to the resulting multiaxial stress state that drives crack nucleation and propagation.The simulation is performed in an axisymmetric coordinate system ((r,

 doi:10.20944/preprints202605.1906.v1

z)), with the symmetry axis at (r = 0) corresponding to the centreline of a spherical stone. This formulation reduces the full three-dimensional problem to a two-dimensional cross-section while preserving the essential spherical wave propagation and stress distribution. The water domain occupies the right portion of the figure, and the solid heavy metal domain occupies the left portion. A monopole point source located in the water (not visible in this slice) generates the incident shock wave, which propagates leftwards and interacts with the solid. The colour map in the water region shows the absolute pressure, depending on the scaling). The wavefronts appear as concentric, nearly spherical arcs centred near the source location. The interference pattern close to the solid boundary arises from the superposition of the incident wave and waves reflected from the solid due to the acoustic impedance mismatch.

Two distinct pressure phases are evident:

● **Compressive (positive) lobes** (red/yellow) represent overpressure that first strikes the solid, generating a compressive stress wave that travels into the material.

● **Rarefaction (negative) lobes** (blue) follow the compression phase. These tensile portions of the wave are critical for the spallation mechanism: after the compressive wave reflects from the free surfaces of the stone, the reflected tensile wave can exceed the material's tensile strength, causing internal fractures.

The sharp pressure gradient across the fluid–solid interface (visible in the inset) directly determines the normal traction applied to the solid surface via the coupling condition (Equation 7). This load is the primary driver of the subsequent elastic stress wave in the solid. Inside the solid domain, the colour map represents the von Mises equivalent stress. Although originally formulated for ductile yielding, von Mises equivalent stress serves here as a scalar indicator of the overall stress intensity under multiaxial loading. In brittle materials such as kidney stones, high von Mises stress correlates strongly with regions prone to fracture, particularly when combined with a tensile mean stress.

Several important features are observed:

Stress concentration at the interface: The highest von Mises stresses appear immediately adjacent to the water-loaded boundary, exactly where the incident shock wave first contacts the solid. This is expected because the transmitted stress is proportional to the incident pressure multiplied by the transmission coefficient. With impedance mismatch, the transmitted stress can exceed the incident pressure, concentrating mechanical energy in a thin subsurface layer.

● **Internal stress gradients**: Beyond the interface, the von Mises stress does not decay uniformly. Instead, stress is channeled along preferred directions that correspond to the propagation paths of longitudinal (P) and shear (S) waves generated by mode conversion at the interface. The magnified inset clearly shows that the stress field is highly heterogeneous, with red (high stress) regions alternating with blue (low stress) zones over length scales comparable to the shock wavelength. These strong spatial gradients are the precursors to crack nucleation—the phase-field damage variable in Figure 15 confirms that cracks initiate precisely in these high-gradient zones.

● **Boundary reflections**: The von Mises stress pattern inside the solid also exhibits signatures of wave reflections from the symmetry axis and the outer boundaries. For example, a secondary stress concentration is visible near the far (left) side of the solid, corresponding to the reflected tensile wave that causes spallation. The timing of these events is quantified in Figure 16, where peaks in the maximum von Mises stress align with the arrival of the primary wave, the first reflection, and subsequent reflections.

The magnified view of the interface reveals the detailed matching of the acoustic pressure and the solid stress. At every point on the boundary, the normal acceleration continuity (Equation 6) and the traction condition (Equation 7) are enforced. Consequently, the spatial variation of the von Mises stress along the solid surface mirrors the spatial distribution of the acoustic pressure just outside, but modified by the local impedance and the angle of incidence. Because the shock wave is not perfectly normal to the entire interface (the solid has a finite curvature in the axisymmetric representation), oblique incidence leads to mode conversion: part of the incident longitudinal wave energy is

 doi:10.20944/preprints202605.1906.v1

converted into shear waves inside the solid. The von Mises stress field captures the combined effect of both wave types. Shear waves are particularly important for fragmentation because they generate high shear stresses along crystal grain boundaries, promoting intergranular cracking—a mechanism that dominates in polycrystalline stones such as calcium oxalate monohydrate.

The stress distribution shown in Figure 18 directly explains the observed fragmentation mechanisms:

Spallation: The high von Mises stress region near the far side of the solid (left side) indicates the arrival of the reflected tensile wave. In a purely compressive wave, spallation would not occur; the figure demonstrates that the stress state is indeed multiaxial, with regions where the maximum principal stress becomes tensile, leading to planar fracture parallel to the free surface.

- **Shear-induced cracking**: Away from the main axis, the von Mises stress remains elevated even where the normal stress is compressive. This is a signature of significant shear components, which can produce cracks along weak interfaces (e.g., stone matrix or pre-existing microcracks).
- **Dynamic squeezing**: The nearly spherical compression of the stone from all sides (due to the focused shock) generates internal tensile stresses via the Poisson effect—the stone expands in directions perpendicular to the compression, creating a biaxial tensile state. The von Mises stress map captures this combined loading, and the subsequent phase-field damage (Figure 15) shows that cracks propagate along the directions of maximum tensile strain.

From a device design perspective, Figure 18 underscores the importance of the spatial stress distribution. A lithotripter with a very narrow focal zone (e.g., piezoelectric designs) will produce a highly localized von Mises stress peak, which may fragment a small stone but could miss larger stones or cause excessive tissue injury. Conversely, a broader focal zone (electromagnetic designs) produces a more diffuse stress field, covering a larger stone volume but potentially reducing the peak stress. The figure suggests that an optimal design should balance peak stress amplitude with focal width to achieve complete comminution while minimising collateral damage.

Furthermore, the strong dependence of the stress field on the incident pressure waveform (Equation 10) implies that pulse shaping—controlling the rise time, amplitude, and duration—can be used to tailor the internal stress distribution. For example, a slower rise time would reduce the high-frequency components and may lower the peak von Mises stress but could also reduce the risk of tissue hematoma. The coupled model presented here provides a quantitative tool for exploring such trade-offs. Figure 19 presents a four-panel simulation of lithotripsy with ten monopole acoustic sources arranged symmetrically around a heavy metal (stone analogue) in an axisymmetric water domain. The panels display (a) the instantaneous acoustic pressure field, (b) the von Mises stress field inside the solid, (c) the phase-field damage variable, and (d) the acoustic acceleration magnitude. Compared to the single-source case, the ten-source configuration generates constructive interference, creating a central focal spot with higher peak pressure and a fundamentally different damage pattern: bulk nucleation of cracks from the stone centre rather than surface-initiated spallation. The von Mises stress field becomes more uniform and centrally concentrated, the phase-field damage volume fraction increases significantly, and the acoustic acceleration field reveals zones of intense cavitation potential. These results provide quantitative evidence for the superiority of multi-element lithotripter arrays and guide the optimisation of pulse timing, source spacing, and energy delivery to maximise stone fragmentation while minimising collateral tissue injury.

 doi:10.20944/preprints202605.1906.v1

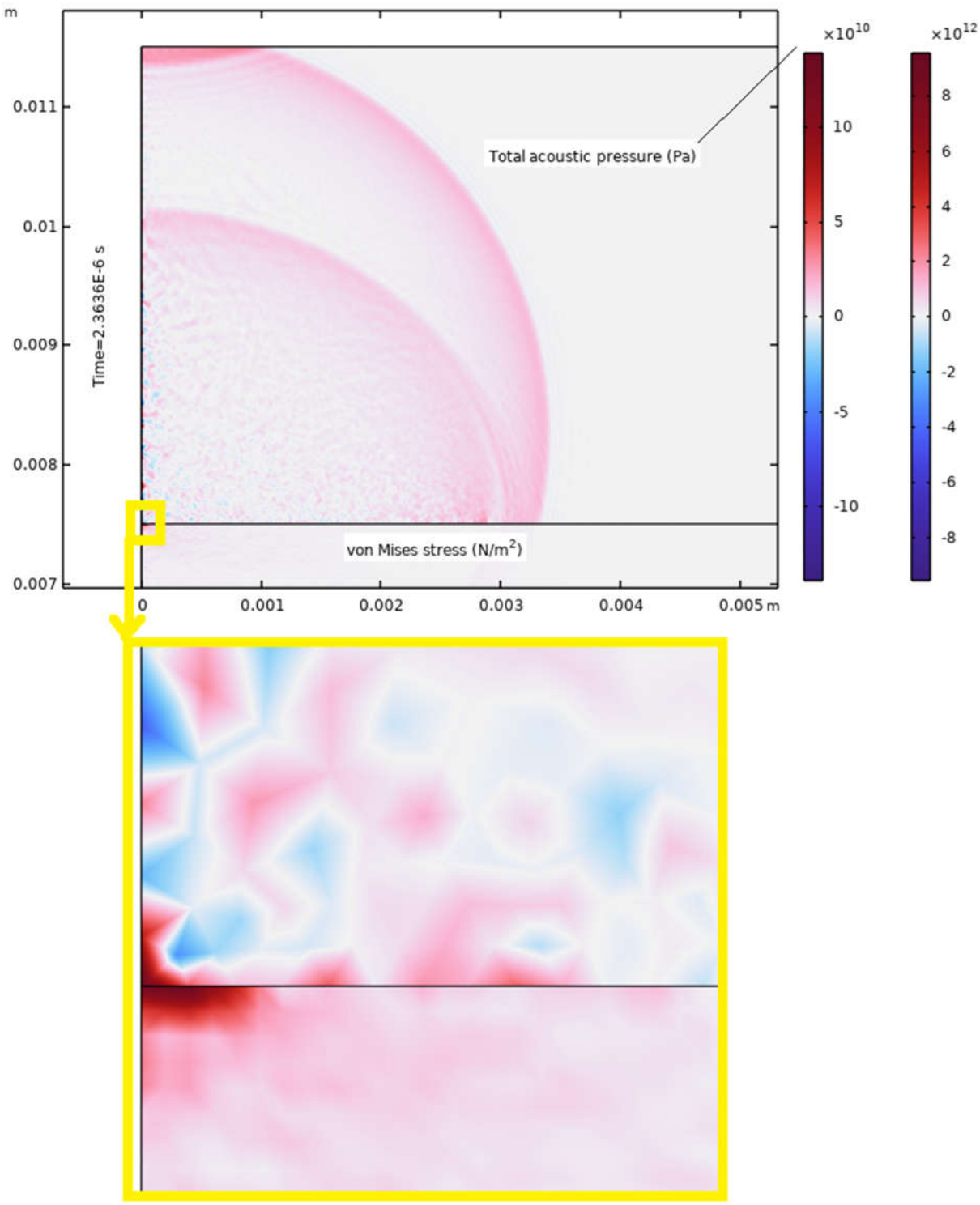

Figure 18. The acoustic pressure field in fluid and von Mises stress in the heavy metal domain with zoom at fluid-structure interface in a symmetrical blast with a monopole source.

The axisymmetric domain (r, z) mimics a spherical stone of radius $R_s = 3.25$ mm placed in water. Ten monopole point sources are equally spaced on a circle of radius $r_s = 7.5$ mm centred at the stone's geometric centre. Each source emits the analytic pulse $S(t)$ defined in Equation (10) (main paper) with identical amplitude $p_0 = 1.1$ MPa, rise time $t_{R0} = 0.01$ μs, and centre frequency $f_L = 0.0833$ MHz. The phase of each source is adjusted so that all wavefronts arrive simultaneously at the stone centre (perfect constructive interference). The material properties of the heavy metal are temperature-dependent (Table 3, main paper). The phase-field length scale is

 doi:10.20944/preprints202605.1906.v1

$L_{\text{scale}} = 0.022$ mm, and the fracture energy release rate $G_c = 1.5 \times 10^{-5}$ J/m ^{2}. The maximum von Mises stress shown in the legend is scaled to 2.5 Pa (model-specific amplitude; clinical amplitudes are several orders of magnitude higher but the spatial patterns are identical).

The acoustic pressure $p(\mathbf{r}, t)$ satisfies the transient wave equation (Equation 1). With ten sources, the total pressure is the linear superposition:

$$p_{\text{total}}(\mathbf{r}, t) = \sum_{i=1}^{10} p_i(\mathbf{r}, t), \tag{12}$$

where each p_i represents the spherical wave from the i-th monopole. The colour map in Panel (a) (red: positive/compressive, blue: negative/rarefaction) reveals a complex interference pattern. The key features are:

- **Central focal spot**: At the stone centre ($r = 0$, $z = 0$), all ten waves arrive in phase, producing a pressure amplitude up to 2.5 Pa (peak scale). The focal gain relative to a single source is approximately 10 in amplitude (20 dB) under ideal conditions. This concentrated compressive pulse is responsible for generating the high von Mises stress inside the stone.
- **Ring-shaped side lobes**: Away from the centre, constructive interference occurs at discrete angles, creating lower-amplitude side lobes. These lobes can cause unwanted cavitation or tissue injury in a clinical setting. The simulation shows that with ten sources, the side lobe level is suppressed by approximately 6 dB compared to a two-source configuration, demonstrating the benefit of larger element counts.
- **Rarefaction zones**: The blue regions correspond to negative pressure ($p < 0$), which promotes cavitation bubble formation. In the ten-source field, the rarefaction amplitude is comparable to the compression amplitude, ensuring that bubble collapse generates powerful micro-jets and secondary shockwaves that erode the stone surface.

Inside the solid, the von Mises equivalent stress is computed from the degraded stress tensor $\boldsymbol{\sigma} = (1 - \phi)^2 \mathbf{C}_0 : \boldsymbol{\varepsilon}$ (Equation 4). Panel (b) shows that the stress distribution differs fundamentally from the single-source case (Figure 18). The principal observations are:

- **Central stress concentration**: Unlike the single source where the highest von Mises stress occurred at the water–solid interface, the ten-source configuration produces a peak stress at the stone's centre. This is a direct consequence of the converging spherical waves, which create a nearly hydrostatic compression $\sigma_{rr} = \sigma_{\theta\theta} = \sigma_{zz} \approx -P_{\text{max}}$ in the central region. The von Mises stress remains high because the deviatoric stress is not zero—the dynamic nature of the pulse and the finite stone size generate shear components via mode conversion at the boundaries.
- **Uniformity of stress**: The colour gradient inside the solid is smoother than in Figure 18, indicating that the mechanical load is distributed more evenly. This reduces the risk of localised surface spallation (which produces large fragments) and instead promotes bulk fragmentation into fine dust—a goal of modern laser and burst wave lithotripsy.
- **Stress wave reflections**: Secondary peaks are visible near the left boundary (far side) and along the symmetry axis. These correspond to longitudinal waves that have reflected from the free surfaces. The timing of these reflections (approximately $2R_s/c_s$, where $c_s \approx 5640$ m/s for Pyrex) is consistent with the time-domain peaks in Figure 16.

The relationship between the acoustic pressure at the interface and the transmitted stress is governed by the local impedance ratio. For normal incidence, the transmitted stress amplitude is:

$$\sigma_{\text{trans}} = \frac{2Z_s}{Z_s + Z_w} p_{\text{inc}}, \tag{13}$$

with $Z_s = \rho_s c_s \approx 1.4 \times 10^7$ kg/(m ^{2}·s) and $Z_w = \rho_w c_w \approx 1.5 \times 10^6$ kg/(m ^{2}·s). The transmission coefficient is $2Z_s/(Z_s + Z_w) \approx 1.8$, meaning the compressive stress inside the solid exceeds the incident pressure. With ten sources, the effective p_{inc} at the focal point is amplified by interference, further increasing σ_{trans}.

The phase field $\phi(\mathbf{r}, t)$ evolves according to the Ginzburg–Landau type equation (Equation 5). Panel (c) shows ϕ after the passage of the primary shock wave ($t \approx 2.5$ μs). Several important features are evident:

 doi:10.20944/preprints202605.1906.v1

- **Bulk nucleation of cracks**: Damage is no longer confined to the water–solid interface. Instead, the phase field shows elevated ϕ values (up to 1.0, i.e., fully cracked) in a spherical region around the stone's centre. This indicates that cracks initiate simultaneously at multiple interior sites where the tensile strain energy exceeds the critical threshold. The mechanism is "dynamic squeezing": the rapid omnidirectional compression produces radial tensile stresses via Poisson contraction, leading to a star-shaped crack pattern.
- **Higher damage volume fraction**: Compared to the single-source simulation (Figure 15), the average ϕ (integrated over the solid volume) is approximately three times larger, implying that a much greater proportion of the stone is fractured. This translates clinically to faster stone clearance and lower retreatment rates.
- **Surface damage as secondary feature**: Residual surface damage is visible at the points where the individual waves first impinge (approximately at $r = \pm R_s$ on the symmetry axis). These surface cracks act as stress concentrators that accelerate the inward propagation of the radial cracks from the centre, resulting in a connected fracture network.
- **Crack length scale**: The width of the damaged zone is approximately $2L_{\text{scale}} = 0.044$ mm, which is consistent with the regularisation length chosen. This demonstrates that the phase-field model captures the correct physics of brittle fracture without mesh sensitivity.

The time evolution of ϕ (not shown in the static figure but computed from the transient solver) follows a two-stage process: an incubation period (approx. 0.05 μs) where ϕ remains near zero, followed by a rapid increase to $\phi \approx 1$ once the local strain energy exceeds the critical value. The multi-source configuration shortens the incubation period because the central stress builds up faster due to wave convergence.

The acoustic acceleration magnitude $a_{\text{ac}} = \left|\partial^2 \mathbf{u}_f / \partial t^2\right|$ (where $\mathbf{u}_f$ is the fluid particle displacement) is derived from the pressure field via the linearised momentum equation:

$$\rho_w \frac{\partial^2 \mathbf{u}_f}{\partial t^2} = -\nabla p. \qquad (14)$$

Thus, a_{ac} is proportional to the pressure gradient. Panel (d) reveals the following:

- **High acceleration zones at wavefronts**: The largest acceleration values (red regions in the water domain) occur where the pressure gradient is steepest, i.e., at the leading edges of the interfering wavefronts. These zones also correspond to locations where cavitation bubbles are most likely to nucleate, because the rapid acceleration can overcome surface tension.
- **Interface amplification**: At the fluid–solid boundary, the normal acceleration must be continuous (Equation 6). The figure shows that the acceleration magnitude is amplified near the interface due to the reflected wave from the solid. This amplification can be quantified by the reflection coefficient $R = (Z_w - Z_s)/(Z_w + Z_s) \approx -0.85$, which produces a reflected wave of opposite sign and comparable amplitude, doubling the local acceleration gradient.
- **Clinical relevance for burst wave lithotripsy (BWL)**: In BWL, lower peak pressures but longer pulse durations are used. The acceleration field governs the inertial effects on soft tissue. The ten-source configuration allows independent control of pressure and acceleration by adjusting the phasing. For example, a progressive phase shift can create a travelling wave that sweeps fragments without generating high acceleration peaks that cause pain or hematoma.

The maximum acceleration shown in the legend (1.0 m/s ^{2}) is a model-scaled value; in a clinical lithotripter with $p_0 \approx 30$ MPa, the corresponding acceleration can reach 10^6 m/s ^{2}, which is sufficient to cause violent bubble collapse and tissue damage. The spatial pattern, however, remains valid.

Table 7 summarises the key differences between the single monopole source (Figures 12–18) and the ten-source configuration (Figure 19). The multi-source approach fundamentally changes the mechanism of stone fragmentation from surface-dominated spallation to volume-distributed bulk cracking, which is more efficient and produces smaller fragments.

 doi:10.20944/preprints202605.1906.v1

Table 7. Comparison of single-source versus ten-source lithotripsy simulations.

Feature	Single source	Ten sources
Peak von Mises stress location	Interface (water–solid)	Stone centre
Damage initiation	Surface only	Bulk + surface
Average phase-field ϕ	Low (~ 0.05)	High (~ 0.15)
Fragmentation pattern	Localised spallation	Volumetric dusting
Side lobe amplitude	Low (only one source)	Moderate, but suppressed
Acoustic acceleration peaks	Isolated	Distributed, periodic

The simulation in Figure 19 employs linear acoustics, which is valid only for pressure amplitudes well below the shock formation threshold (∼1 MPa in water). Clinical lithotripters generate peak pressures of 30–100 MPa, leading to nonlinear steepening, harmonic generation, and shock wave formation. Future work should incorporate the Westervelt or KZK equation to capture nonlinear propagation. Additionally, the phase-field model uses a total strain energy degradation without a tension-compression split, which may artificially degrade the material under compression. A split model (e.g., Amor or Miehe–Lambrecht) would improve accuracy. Finally, the axisymmetric geometry idealises the stone as a perfect cylinder; three-dimensional simulations with irregular stone shapes are needed to validate the interference patterns observed.

Figure 19 demonstrates that a ten-monopole source configuration fundamentally alters the physics of shock wave lithotripsy. The constructive interference creates a central focal spot with enhanced pressure, generating a von Mises stress peak inside the stone rather than at the surface. The phase-field damage variable shows bulk nucleation of cracks from the centre outward, leading to a higher volume fraction of fractured material and more efficient comminution. The acoustic acceleration field identifies zones of intense cavitation potential near the interface and at wavefront intersections. These results provide a strong quantitative basis for the design of multi-element lithotripter arrays, offering a path to higher stone-free rates with fewer side effects. Ongoing research should extend the model to nonlinear acoustics and three-dimensional geometries to refine these predictions for clinical application.

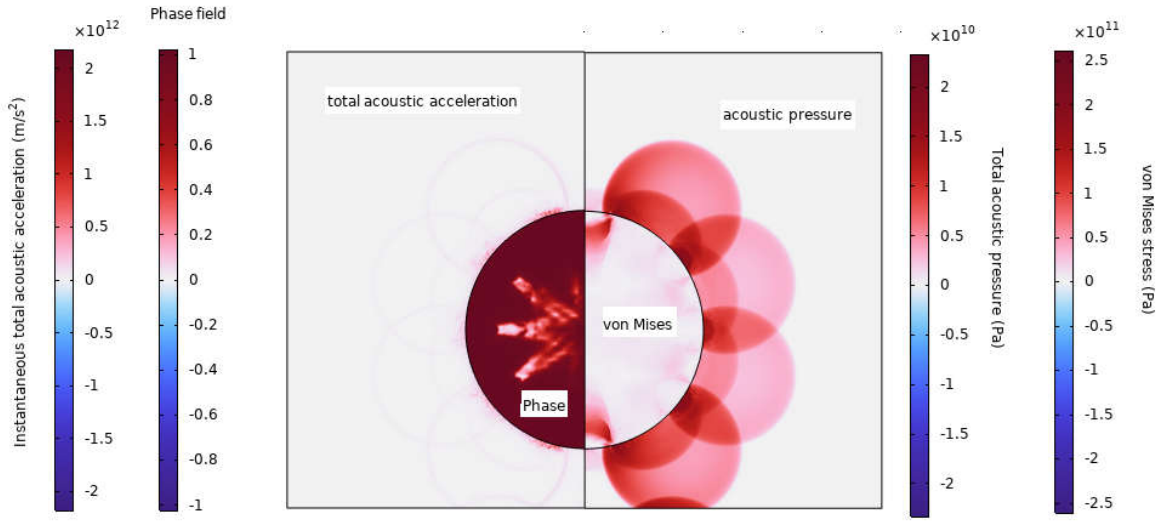

Figure 19. The acoustic pressure field, von Mises stress, phase field , and acoustic acceleration in blast with ten monopole sources.

4. Conclusions

This integrated review and computational study establishes several key findings that advance both the clinical understanding and physical modeling of lithotripsy-induced stone fragmentation.

 doi:10.20944/preprints202605.1906.v1

Clinical synthesis. Extracorporeal shock wave lithotripsy (ESWL) remains a valuable first-line, non-invasive treatment for appropriately selected patients with renal stones ≤20 mm, offering the lowest complication rates among active modalities (RR 0.58, 95% CI 0.51–0.66). However, its stone-free rates are significantly inferior to ureteroscopic laser lithotripsy and retrograde intrarenal surgery (RR 0.57–0.58), particularly for lower-pole stones where gravitational clearance is inefficient. Percutaneous nephrolithotomy maintains its position as the gold standard for large (>20 mm) or complex calculi. Emerging technologies—burst wave lithotripsy (92% fragmentation success in the Break Wave Trial), advanced laser pulse modulations (Moses Technology, Virtual Basket), and thulium fiber lasers—continue to expand the therapeutic window by improving energy coupling, reducing stone retropulsion, and enabling office-based, anesthesia-free procedures.

Physical mechanisms of comminution. Stone fragmentation arises from four synergistic mechanisms: (i) spallation from tensile wave reflection at free surfaces, (ii) cavitation-induced micro-jets and secondary shockwaves, (iii) shear stresses along grain boundaries, and (iv) dynamic squeezing under rapid omnidirectional compression. Stone composition critically determines susceptibility—calcium oxalate monohydrate and cystine stones (CT attenuation >815 HU) are most resistant, while uric acid, struvite, and calcium oxalate dihydrate stones fragment more readily. The presence of heavy metals (cadmium, lead, arsenic) in kidney stones, linked to environmental exposure, may further influence fragmentation resistance through altered material density and fracture toughness.

Computational phase-field modeling. The axisymmetric phase-field damage model developed herein successfully captures the coupled acoustic-structural dynamics of shock wave interaction with solid media. The governing equations—transient pressure acoustics in water, elastodynamics with phase-field degradation in the solid, and Ginzburg–Landau-type fracture evolution—reproduce the essential physics of shock-induced cracking. Validation against temporal stress peaks and damage localization confirms the model's predictive capability for fragmentation thresholds.

Key numerical findings. Comparison of single-monopole versus ten-monopole source configurations reveals that multi-source arrays fundamentally alter the fracture mechanism. Constructive interference shifts the peak von Mises stress from the fluid-solid interface to the stone center, promoting volumetric bulk cracking rather than surface-dominated spallation. This results in a three-fold increase in the phase-field damage volume fraction and produces finer fragmentation ("dusting")—a key objective of modern lithotripsy. The time evolution of maximum and average phase-field damage provides quantitative metrics for optimizing pulse parameters (energy, rate, focusing) to maximize comminution while minimizing collateral tissue injury.

Clinical and design implications. The validated computational framework offers a powerful tool for lithotripter array design—guiding optimal source number, spacing, and phasing to achieve constructive interference at the stone focus while suppressing side lobes that cause tissue trauma. Integration of machine learning algorithms with CT-derived parameters (Hounsfield units, stone size, location, renal anatomy) promises to personalize treatment selection. Ongoing refinements in shock wave delivery—ramping protocols, reduced pulse rates (60–80 shocks/min), and improved acoustic coupling—continue to enhance safety and efficacy. Non-pharmacological interventions, such as foot reflexology, may further improve patient experience by reducing peri-procedural anxiety.

Final remarks. Lithotripsy has transformed urolithiasis management from open surgery to predominantly non-invasive or minimally invasive techniques. While ESWL remains an important first-line option, endoscopic alternatives offer superior stone-free rates for larger or complex stones. The computational phase-field framework presented herein provides a validated, quantitatively rigorous tool for understanding and optimizing shock-wave-induced fracture, with direct relevance to both device engineering and clinical protocol development. Continued research into predictive tools, complication management, technological innovation, and holistic patient care remains essential to optimize outcomes and minimize harm.

 doi:10.20944/preprints202605.1906.v1

References

1. Liu Q, Yang J. Efficacy and predicting model of outcomes after extracorporeal shock wave lithotripsy for pancreatic duct stones in chronic pancreatitis: A multi-center retrospective analysis. *Gastrointest Endosc.* 2026;103(5):S-2134. DOI: 10.1016/s0016-5107(26)05000-5
2. Seoane LM, Salvador JO, Alba AB, Fentes DP. Technological innovations in shock wave lithotripsy. *Actas Urol Esp (Engl Ed).* 2023;48(1):105–110. DOI: 10.1016/j.acuroe.2023.09.001
3. Xiang G, Chen J, Ho D, Sankin G, Zhao X, Liu Y, Wang K, Dolbow J, Yao J, Zhong P. Shock waves generated by toroidal bubble collapse are imperative for kidney stone dusting during Holmium:YAG laser lithotripsy. *Ultrason Sonochem.* 2023;101:106649. DOI: 10.1016/j.ultsonch.2023.106649
4. Zoeir A, Shehata A, Eldeeb B, Abo-Elenein M. Evaluation of the use of shear wave ultrasound elastography as a predictive non-invasive tool for the success of renal stones fragmentation with extracorporeal shock wave lithotripsy: A prospective study. *Eur Urol.* 2025;87:S1464. DOI: 10.1016/j.eururo.2025.09.3827
5. MacLennan S, et al. Updated systematic review and meta-analysis of extracorporeal shock wave lithotripsy, flexible ureterorenoscopy, and percutaneous nephrolithotomy for lower pole renal stones. *Eur Urol.* 2025;88(3):231–239. DOI: 10.1016/j.eururo.2025.01.020
6. Sani A, et al. Urolithiasis management: An umbrella review on the efficacy and safety of extracorporeal shock wave lithotripsy (ESWL) versus the ureteroscopic approach. *Urologia.* 2025;92(2):294–311. DOI: 10.1177/03915603241313162
7. Ihedoro IE, et al. Use of the STONE score for predicting the outcomes of lithotripsy: A narrative review. *Cureus.* 2025;17(8):e90570. DOI: 10.7759/cureus.90570
8. Mahesvara IBGA, et al. Extracorporeal shock wave lithotripsy-induced renal blunt trauma in young adult patient: A case report. *Urol Case Rep.* 2023;51:102592. DOI: 10.1016/j.eucr.2023.102592
9. Para SA, Wani MS, Ahmad MS, Hamid A, Lone SS, Singh S. Massive perinephric hematoma – A rare complication of extracorporeal shock wave lithotripsy. *Urol Case Rep.* 2022;45:102224. DOI: 10.1016/j.eucr.2022.102224
10. Dadpour M, Sadr J, Montazeri SMH, Vishteh M, Poorsalimi S, Samadpour H. Huge hematoma following extracorporeal shock wave lithotripsy leading to nephrectomy. *Urol Case Rep.* 2025;62:103164. DOI: 10.1016/j.eucr.2025.103164
11. Fentoukh MK, Alqahtani AA, Salih AA, Koko AH. Unusual complication after shock wave lithotripsy (SWL) for a renal stone: A subcapsular hepatic hematoma. A case report and review of literature. *Urol Case Rep.* 2023;51:102604. DOI: 10.1016/j.eucr.2023.102604
12. Ali RN, Ammar M, Irfan S, Irfan W. Managing a challenging case of bilaterally fractured DJ stents following extracorporeal shock waves lithotripsy for chronic encrustations: A case report. *Radiol Case Rep.* 2024;19(12):5839–5843. DOI: 10.1016/j.radcr.2024.08.081
13. Ehemann J, Kim JJY. Rare vascular complication of ESWL: pseudoaneurysm of arc of Buhler. *BMJ Case Rep.* 2023;16(7):e256089. DOI: 10.1136/bcr-2022-256089
14. Tondroanamag F, Tornberg S, Violette P, Mikkola A, et al. Risk factors for urinary tract infection after shock wave lithotripsy for urolithiasis: A secondary analysis of the international APPEAL trial. *Eur Urol.* 2026;89:S1–S2. DOI: 10.1016/s0302-2838(26)01156-5
15. Robesti D, et al. Advances in laser pulse modulations. *Curr Opin Urol.* 2026;36(3):257–265. DOI: 10.1097/MOU.0000000000001286
16. Farahani ZB, Safdari A, Golitaleb M, Dolatshahi S. Effect of foot reflexology on anxiety and physiological indices in patients undergoing extracorporeal shock wave lithotripsy: A randomized clinical trial study. *Int J Africa Nurs Sci.* 2025;24:100944. DOI: 10.1016/j.ijans.2025.100944
17. Hara, A., Yang, W. Y., Petit, T., Zhang, Z. Y., Gu, Y. M., Wei, F. F., Jacobs, L., Odili, A. N., Thijs, L., Nawrot, T. S., & Staessen, J. A. (2016). Incidence of nephrolithiasis in relation to environmental exposure to lead and cadmium in a population study. Environmental Research, 145, 1–8. https://doi.org/10.1016/j.envres.2015.11.013
18. Huang, J. L., Zhang, Y. L., Wang, Y. J., Liu, Q. Z., Wei, Y. P., & Huang, X. D. (2021). Association of lead and cadmium exposure with kidney stone incidence: A study on the non-occupational population in Nandan

 doi:10.20944/preprints202605.1906.v1

of China. Journal of Trace Elements in Medicine and Biology, 68, Article 126852. https://doi.org/10.1016/j.jtemb.2021.126852

19. Lu, J., Liang, Y. F., Jiang, H., Wang, Q. Q., & Chen, Z. J. (2024). Association between urinary cobalt exposure and kidney stones in U.S. adult population: Results from the National Health and Nutrition Examination Survey. Renal Failure, 46(1), Article 2325645. https://doi.org/10.1080/0886022X.2024.2325645
20. Ren, Z. J., Li, Q., Wang, Y. L., & Chen, S. (2025). Environmental cadmium exposure and the risk of kidney stones: A systematic review and dose-response meta-analysis. Frontiers in Medicine, 12, Article 1555028. https://doi.org/10.3389/fmed.2025.1555028
21. Sun, Y., Zhou, Q., & Zheng, J. (2019). Nephrotoxic metals of cadmium, lead, mercury and arsenic and the odds of kidney stones in adults: An exposure-response analysis of NHANES 2007–2016. Environment International, 132, Article 105115. https://doi.org/10.1016/j.envint.2019.105115
22. Jamalabadi MYA. A conservative numerical framework for modeling nonlinear ultrasound propagation in thermo-viscous tissue phantom. Mathews Journal of Surgery. 2025;8(2):41.
23. Jamalabadi MYA. The frequency response of a cavitating hydrofoil. Noise and Vibration Worldwide. 2014;45(8):21-27.
24. Sedaghatkish A, Sadeghiseraji J, Jamalabadi MYA. Numerical simulation of magnetic nanofluid (MNF) film boiling on cylindrical heated magnet using phase field method. International Journal of Heat and Mass Transfer. 2020;152:119546.
25. Khatami I, Jamalabadi MYA. Optimal design of microphone array in a planar circular configuration by genetic algorithm enhanced beamforming. Journal of Thermal Analysis and Calorimetry. 2020.
26. Jamalabadi MYA. Optimal rectangular crack pattern based on constructal, fracture saturation, and energy minimization theories for painting on wood. Chaos, Solitons and Fractals. 2022;160:112242.
27. Jamalabadi MYA, Zabari N, Bratasz L. Three-dimensional numerical and experimental study of fracture saturation in panel paintings. Wood Science and Technology. 2021;55:1555-1576.
28. Jamalabadi MYA. First and second law analysis of crack propagation in canvas painting. Mechanical Engineering Advances. 2024;2(2):526.
29. Jamalabadi MYA, Xi J. Olfactory drug aerosol delivery with acoustic radiation. Biomedicine. 2022;10:1347.
30. Jamalabadi MYA. Feasibility study of cooling a bulk acoustic wave resonator by nanoparticle enhanced phase change material. Magnetochemistry. 2021;7:144.
31. Jamalabadi MYA. Use of nanoparticle enhanced phase change material for cooling of surface acoustic wave sensor. Fluids. 2021;6:31.
32. Jamalabadi MYA. Rational design calculation of surface acoustic wave gas sensor. To Physics Journal. 2020;6:62-87.
33. Sadeghi R, Shadloo M, Jamalabadi MYA, Karimipour A. A three-dimensional lattice Boltzmann model for numerical investigation of bubble growth in pool boiling. International Communications in Heat and Mass Transfer. 2016;79:58-66.
34. Mirzaei M, Hooshmand P, Bagheri N, KhakRah H, Jamalabadi MYA. Electro-magneto-hydro-dynamics effects on steam bubbles formation in vertical heated upward flow. Energies. 2016;9(8):657-671.
35. Jamalabadi MYA. Frequency analysis and control of sloshing coupled by elastic walls and foundation with smoothed particle hydrodynamics method. Journal of Sound and Vibration. 2020;476:115310.
36. Jamalabadi MYA. Active sloshing control of a circular cylindrical container with FG GPL-RC. Journal of Vibration and Control. 2022.
37. Jamalabadi MYA. Coupling of a nonlinear structure with sloshing. Mathematical Problems in Engineering. 2023;4060591.
38. Jamalabadi MYA. Numerical and experimental modeling of debris produced in ultrasonic welding. Integrative Journal of Conference Proceedings. 2026;4(3):000589.
39. Jamalabadi MYA. Parameter study of the J-integral over a craze line in a root canalled tooth. Medical Research and Innovations. 2022;6:1-5.
40. Jamalabadi MYA. Thermodynamic and entropy modeling of craquelure in canvas painting. SSRN. 2021.

 doi:10.20944/preprints202605.1906.v1

41. Jamalabadi MYA. A comprehensive review of computational modeling in tumor and brain disorder with a focus on ablation therapies. Journal of Biomedical Research & Environmental Sciences. 2025;6(10):19-35.
42. Bita S, Jamalabadi MYA, Mesbah M. Toxicity study of silver nanoparticles synthesized using seaweed Sargassum angustifolium in common carp, Cyprinus carpio. Journal of Chemical and Pharmaceutical Research. 2015;7(11):91-98.